Variationally consistent homogenisation of plates

Available online at www.sciencedirect.com
ScienceDirect
Comput. Methods Appl. Mech. Engrg. 413 (2023) 116094
Computer methods in applied mechanics and engineering
www.elsevier.com/locate/cma

Variationally consistent homogenisation of plates

Elias Börjesson[a,*], Fredrik Larsson[a], Kenneth Runesson[a], Joris J.C. Remmers[b], Martin Fagerström[a]

[a] Department of Industrial and Materials Science, Chalmers University of Technology, Gothenburg, Sweden
[b] Department of Mechanical Engineering, Eindhoven University of Technology, Eindhoven, The Netherlands

Received 22 December 2022; received in revised form 26 April 2023; accepted 26 April 2023
Available online 3 June 2023

Abstract

Advanced fibre composite materials are often used for weight-efficient thin-walled designs, making a plate-based modelling approach suitable for their structural assessment. However, as the sub-structural geometrical features of these materials govern much of their behaviour, a multi-scale approach is necessary. A related challenge, however, is that the in-plane variation of these sub-structural features may be much larger than the total thickness of the material, whereby tailored homogenisation techniques for shell elements are needed. Existing frameworks for plate- and shell-based homogenisation are typically developed using second-order homogenisation in combination with the Hill–Mandel (macro-homogeneity) condition. However, it has been reported in the literature that this approach can lead to kinematic inconsistencies in the macro- to micro-scale transition. One inconsistency that is commonly reported, is the inability to correctly account for the macro-scale transverse shear behaviour on the sub-scale level. In this contribution, we show how the method of Variationally Consistent Homogenisation (VCH) can be used to develop a homogenisation framework for Reissner-Mindlin plate elements, which guarantees kinematically consistent prolongation and homogenisation operations. The homogenisation approach is demonstrated in four numerical examples, where it is shown that the method accurately homogenise the effective sectional plate stiffnesses of homogeneous and heterogeneous sub-structures.

Keywords: Multi-scale modelling; Variationally consistent homogenisation; Composites; Plates

1. Introduction

The development of novel materials often lead to innovative composites with intricate structure on the meso- or micro-scopic level. This is especially evident in, e.g. advanced fibre-reinforced polymers, where sub-scale heterogeneities often appear as complex geometrical formations of multiple material constituents. While the increased complexity of the sub-scale structure often leads to improved structural behaviour or increased functionality, the simulation and analysis process of these materials becomes more challenging. Since the structural assessment needs to be analysed on a scale with dimensions far superseding that of the material sub-structure, it is important to develop multi-scale modelling approaches where the properties of the sub-scale can be accounted for.

* Corresponding author.
E-mail address: elias.borjesson@chalmers.se (E. Börjesson).

https://doi.org/10.1016/j.cma.2023.116094

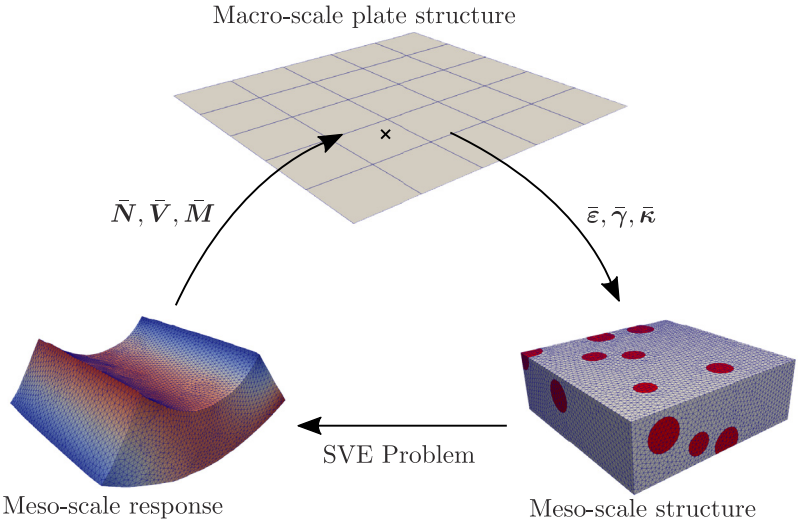

Fig. 1. Illustration of plate-based computational homogenisation. The kinematic plate deformations (elongation $\bar{\boldsymbol{h}}$, transverse shear $\bar{\boldsymbol{g}}$, curvature $\bar{\boldsymbol{\kappa}}$) are prolonged (down-scaled) to the SVE. The resulting sectional forces (membrane $\bar{\boldsymbol{N}}$, transverse shear $\bar{\boldsymbol{V}}$ and bending $\bar{\boldsymbol{M}}$) and stiffnesses on the SVE level are then homogenised (up-scaled) and used as constitutive relations for the macro plate element.

Furthermore, novel materials are often developed with lightweight design in mind. In these cases, (thin) structural components such as beams, plates or shells are common design elements. In industry, the structural behaviour of these components are usually analysed with appropriate structural finite elements, due to the substantially better computational performance compared to resolving the component with continuum (solid) elements.

With the prominent usage of structural finite elements in industry, and a clear need to include multi-scale effects in the simulation models, there is a desire to develop general multi-scale procedures in which the largest scale is represented with structural finite elements. In recent years, a number of such multi-scale methods has been proposed for beams, cf. e.g. [1,2], and plates/shells, cf. e.g. [3–9]. In the majority of the listed citations, the authors base their multi-scale methods on computational homogenisation (also commonly referred to as FE^2) [10,11], see Fig. 1 for an illustration. In this technique, the structural component is discretised with plate elements, for which each quadrature point (on the macro-scale) is associated with a unique finite element model of a Statistical Volume Element[1] (SVE) that represents the sub-scale features. The two scales are then linked via a set of prolongation and homogenisation conditions, whereby the macro-scopic shell kinematical quantities (elongation, curvature and (possibly) transverse shear deformation), are down-scaled to the SVE, and where homogenised macro-scale kinematic quantities (section forces and moments), are up-scaled to the macro-scopic shell element.

The computational effort required by FE^2 approaches is (in the fully non-linear regime) substantial, as each quadrature point in the macro-scopic model includes its own FE-problem. Although the computational demand for FE^2 simulations are much lower compared to the corresponding fully resolved problem, the use of multi-scale approaches based on FE^2 are in most cases not feasible for industrial applications. However, the use of computational homogenisation does have practical applications in areas such as virtual testing, or upscaling of effective material properties from heterogeneous materials. The latter can be adopted whenever the underlying problem is fully linear, which is the case studied in this paper.

In the beam and shell-based computational homogenisation methods currently found in the literature, second-order homogenisation is commonly used to include higher-order deformations modes, e.g. bending, on the SVE level [12]. Moreover, the Hill–Mandel macro-homogeneity condition is used to enforce energy equivalence between the scales. However, as shown by authors in e.g. [1,13,14], this can often lead to kinematical inconsistencies between the macro- and micro-scales. For example, Främby et al. [14] showed that if no special consideration is taken for the transverse shear behaviour, the homogenisation and prolongation operations will fail to accurately capture the

[1] The sub-scale models are often referred to as Representative Volume Elements (RVEs). However, a sample of the sub-structure will, in general, not be truly representative, whereby we prefer the term Statistical Volume Element.

transverse shear stiffness. More specifically, the volume-averaged transverse shear angle on the SVE-level tends to diverge from the macro-scopic shear angle.

As a consequence, additional constraints for the boundary value problem on the SVE level needs to be devised, in order to ensure kinematical consistency between the two scales. For example, regarding the inconsistent transverse shear behaviour previously discussed, Geers et al. [4] proposed additional constraints enforcing the average angle on the lateral faces (of the SVE). This was demonstrated to work well for SVE sizes with aspect ratios close to one, but larger in-plane to out-of-plane aspect ratios were not analysed.

In a related work, Hii et al. [9] developed a homogenisation framework for Reissner-Mindlin type shells. In order to enforce kinematical consistency between the scales, they used a set of orthogonality conditions previously developed by Luscher et al. [15], out of which the most influential condition requires that the volume-averaged sub-scale displacements contributed by the fluctuation field is orthogonal to the contributions from the macro-scopic second gradient of the displacements. However, when loosening these conditions to fulfil traction equivalence on the upper and lower surface of the shell, Hii et al. still encountered issues related to transverse shear behaviour. As a result, an additional volumetric constraint to enforce a volume averaged transverse shear angle throughout the SVE domain was added. This resulted in an efficient down-scaling and up-scaling procedure that correctly homogenises the macro-scopic membrane, bending, and transverse shear stiffnesses adequately.

More recently, Müller et al. [16] developed a homogenisation approach for beams and plates, based on first order homogenisation with Irving–Kirkwood theory, that did not show any sign of the aforementioned erroneous size dependence for the transverse shear behaviour. However, the resulting stresses in the transverse direction (for the SVE problem) were dependent on the shape of a predetermined ansatz function. Furthermore, the SVE problem was only formulated with Dirichlet boundary conditions, and was not demonstrated to work with periodic boundary conditions.

In conclusion, although recent developments show great promise, there is still a need for a general approach for developing multi-scale methods, that guarantees consistent prolongation and homogenisation through the scales, and that is free both from a-priori assumptions on the macro- and sub-scale, and from a-posteriori additional constraints to compensate for erroneous responses. To address this, in this paper we propose a computational homogenisation approach based on Variationally Consistent Homogenisation (VCH) [17].

VCH has the attractive property of not requiring any a-priori specification or knowledge of the macro- or subscale (SVE) problems. Instead, both problems are derived from a single, fully resolved problem, which gives rise to a consistent basis for multi-scale methods. VCH was first introduced in 2010 by Larsson et al. [17], and has since then been successfully applied to a number of different problems, for example homogenisation of damage and fracture [18,19], homogenisation of multi-physics systems [20], and chemo-mechanical problems [21]. Furthermore, in a related work, VCH was recently used to develop a homogenisation procedure for Timoshenko beam elements [2,22], where it was shown that the correct membrane, bending and transverse shear behaviour could be properly captured.

In this paper, the VCH method will be applied to plate elements formulated with Reissner-Mindlin theory. Note, however, that this is only for demonstration purposes and any kinematic plate theory could be used. As a result, we will show how equations for consistent down-scaling and up-scaling of plate properties naturally arise from the formulation. Moreover, it will be shown that when using the VCH method, a minimum set of constraints for the sub-scale boundary value problem are automatically derived.

The reminder of this paper is organised as follows. First an outline of the VCH approach will be presented in Section 2, including the development of the prolongation and homogenisation procedure. In Sections 3 and 4, the boundary value problem for the macro-scale and SVE problems will be established. In Section 5, four numerical examples will be presented to demonstrate the capabilities of the proposed framework. Finally, the findings in the paper will be summarised and discussed in Section 6.

2. VCH of plates

VCH is adopted in order to derive a computational framework for Reissner-Mindlin plate elements. The main steps in the VCH method are:

- Define the single scale problem where any heterogeneities are fully resolved.

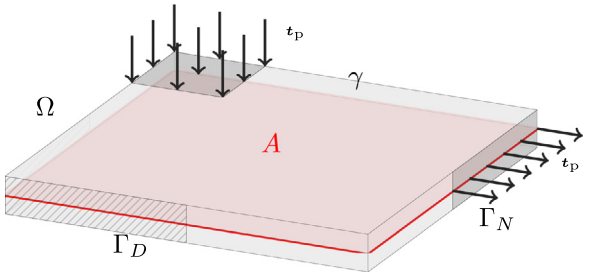

Fig. 2. Plate occupying the three-dimensional domain Ω. Its mid-plane occupies the two-dimensional surface A.

- Decompose the displacement field into macro-scale and sub-scale (fluctuation) components in accordance with the variational multi-scale method [23].
- Restate the weak form by applying local domain averaging.
- Develop the prolongation and homogenisation conditions to link the macro- and sub-scales.
- Establish the boundary value problems for the macro-scale plate elements and the SVE sub-structure.

These steps will be described in detail in the following sub-sections.

2.1. The fully resolved problem

Consider the plate in Fig. 2, and let Ω denote its three-dimensional volume, while A denotes the mid-surface. The boundary of the plate is composed of the upper and lower surfaces γ, and an edge surface, Γ. The boundary surface Γ can be further divided into boundaries subjected to Dirichlet conditions, Γ_{D}, and Neumann conditions, Γ_{N}. Furthermore, the plate is subjected to prescribed boundary tractions $\boldsymbol{t}_{\mathrm{p}}$ on the boundaries γ and Γ_{N}. To simplify the analysis (and to avoid technical difficulties that may cloud the main message of the paper), we take the plate thickness, t, as constant. In addition, we ignore body loads.

With the above definitions in place, the standard weak format of the elasticity problem can be formulated: Find $\boldsymbol{u} \in \mathbb{U}$ such that:

$$\int_{\Omega} \boldsymbol{\sigma}(\boldsymbol{\epsilon}[\boldsymbol{u}]) : \boldsymbol{\epsilon}[\delta\boldsymbol{u}]\mathrm{d}\Omega = \int_{\gamma} \boldsymbol{t}_{\mathrm{p}} \cdot \delta\boldsymbol{u}\mathrm{d}\Gamma + \int_{\Gamma_N} \boldsymbol{t}_{\mathrm{p}} \cdot \delta\boldsymbol{u}\mathrm{d}\Gamma \quad \forall \delta\boldsymbol{u} \in \mathbb{U}^0, \tag{1}$$

where $\boldsymbol{\sigma}$ is the Cauchy stress tensor, and $\boldsymbol{\epsilon}[\boldsymbol{u}] = [\boldsymbol{u} \otimes \boldsymbol{\nabla}]^{\mathrm{sym}}$ is the strain tensor defined for small deformations. Furthermore, the trial set $\mathbb{U}$ and the test space $\mathbb{U}^0$ are defined as follows:

$$\mathbb{U} = \{\boldsymbol{u} \in \mathbb{H}^1(\Omega) | \boldsymbol{u} = \boldsymbol{u}_{\mathrm{p}} \text{ on } \Gamma_{\mathrm{D}}\}, \tag{2}$$

$$\mathbb{U}^0 = \{\boldsymbol{u} \in \mathbb{H}^1(\Omega) | \boldsymbol{u} = \boldsymbol{0} \text{ on } \Gamma_{\mathrm{D}}\}, \tag{3}$$

where $\mathbb{H}^1(\Omega)$ denotes the Sobolev space of functions with square integrable functions and gradients on Ω.

2.2. Decomposition of functions

Next, we adopt the idea from the variational multi-scale method [23], where we assume that any field in the domain Ω can be uniquely decomposed as a sum of contributions coming from the macro- and sub-scale (here denoted with superscripts $\bullet^{\mathrm{M}}$ and $\bullet^{\mathrm{s}}$, respectively):

$$\boldsymbol{v} = \boldsymbol{v}^M + \boldsymbol{v}^{\mathrm{s}}, \quad \boldsymbol{v} \in \mathbb{H}^1(\Omega). \tag{4}$$

Introducing this decomposition for the displacement field, i.e. $\boldsymbol{u} = \boldsymbol{u}^M + \boldsymbol{u}^{\mathrm{s}}$, into the fully resolved problem in Eq. (1), we obtain the equivalent (two-scale) problem of finding $\boldsymbol{u}^M \in \mathbb{U}^{\mathrm{M}}$ and $\boldsymbol{u}^{\mathrm{s}} \in \mathbb{U}^{\mathrm{s}}$ such that:

$$\int_{\Omega} \boldsymbol{\sigma}(\boldsymbol{\epsilon}[\boldsymbol{u}^{\mathrm{M}} + \boldsymbol{u}^{\mathrm{s}}]) : \boldsymbol{\epsilon}[\delta\boldsymbol{u}^{\mathrm{M}}]\mathrm{d}\Omega = \int_{\gamma} \boldsymbol{t}_{\mathrm{p}} \cdot \delta\boldsymbol{u}^{\mathrm{M}}\mathrm{d}\Gamma + \int_{\Gamma_N} \boldsymbol{t}_{\mathrm{p}} \cdot \delta\boldsymbol{u}^{\mathrm{M}}\mathrm{d}\Gamma \quad \forall \delta\boldsymbol{u}^{\mathrm{M}} \in \mathbb{U}^{\mathrm{M},0}, \tag{5}$$

$$\int_{\Omega} \boldsymbol{\sigma}(\boldsymbol{\epsilon}[\boldsymbol{u}^{\mathrm{M}} + \boldsymbol{u}^{\mathrm{s}}]) : \boldsymbol{\epsilon}[\delta \boldsymbol{u}^{\mathrm{s}}] \mathrm{d}\Omega = \int_{\gamma} \boldsymbol{t}_{\mathrm{p}} \cdot \delta \boldsymbol{u}^{\mathrm{s}} \mathrm{d}\Gamma \quad \forall \delta \boldsymbol{u}^{\mathrm{s}} \in \mathbb{U}^{\mathrm{s}}. \tag{6}$$

Note that we restrict ourselves to only consider volumetric homogenisation, whereby we set $\boldsymbol{u}^{\mathrm{s}} = 0$ on Γ in Eq. (6). Thereby, the Dirichlet conditions in $\mathbb{U}$ are imposed through $\mathbb{U}^{\mathrm{M}}$, motivating the test space $\mathbb{U}^{\mathrm{M},0}$ in Eq. (5).

2.3. Local domain averaging

As the next step towards replacing the fully resolved problem with a multi-scale formulation, we introduce running averages on the mid-surface A. This amounts to first introducing the SVE-domains $\Omega_{\square}$ inside the domain Ω, see Fig. 3(a) where $\gamma_{\square}$ is used to denote the top and bottom boundaries of the SVE, and $A_{\square}$ to denotes the mid-surface of the SVE domain. Note that the SVE-domain $\Omega_{\square}$ covers the entire thickness of the plate. As such, there is no separation of scale in the thickness direction.

To introduce the local domain averaging, we assume that any integrand can be restated by their running averages as:

$$\begin{aligned} \int_{\Omega} f \mathrm{d}\Omega &\approx \int_{A} \frac{1}{A_{\square}} \left[\int_{\Omega_{\square}} f \mathrm{d}\Omega \right] \mathrm{d}A = \int_{A} \langle f \rangle_{\square} \mathrm{d}A \\ \int_{\gamma} g \mathrm{d}\Gamma &\approx \int_{A} \frac{1}{A_{\square}} \left[\int_{\gamma_{\square}} g \mathrm{d}\Gamma \right] \mathrm{d}A = \int_{A} \langle g \rangle_{\square}^{\gamma} \mathrm{d}A \end{aligned} \tag{7}$$

where we have introduced the domain averages:

$$\langle \bullet \rangle_{\square} = \frac{1}{A_{\square}} \int_{\Omega_{\square}} \bullet \mathrm{d}\Omega \mathrm{d}A, \qquad \langle \bullet \rangle_{\square}^{\gamma} = \frac{1}{A_{\square}} \int_{\gamma_{\square}} \bullet \mathrm{d}\Omega \mathrm{d}A, \tag{8}$$

where $\Omega_{\square}$ and $A_{\square}$ are defined for each point $\bar{\boldsymbol{x}} \in A$ such that $\frac{1}{A_{\square}} \int_{A_{\square}} \boldsymbol{x} \mathrm{d}A = \bar{\boldsymbol{x}}$, i.e. $\bar{\boldsymbol{x}}$ is the centroid of each SVE. Note that for two sufficiently close points in A, the SVE-domains will overlap, whereby Eq. (7) only represents an approximation. In practice, however, the approximation is still accurate under the assumption of separation of scale.

Introducing the domain averaging in Eq. (7) into Eqs. (5) and (6), we obtain the following two equations:

$$\int_{A} \langle \boldsymbol{\sigma}(\boldsymbol{\epsilon}[\boldsymbol{u}^{\mathrm{M}} + \boldsymbol{u}^{\mathrm{s}}]) : \boldsymbol{\epsilon}[\delta \boldsymbol{u}^{\mathrm{M}}] \rangle_{\square} \mathrm{d}A = \int_{A} \langle \boldsymbol{t}_{\mathrm{p}} \cdot \delta \boldsymbol{u}^{\mathrm{M}} \rangle_{\square}^{\gamma} \mathrm{d}A + \int_{\Gamma_N} \boldsymbol{t}_{\mathrm{p}} \cdot \delta \boldsymbol{u}^{\mathrm{M}} \mathrm{d}\Gamma \quad \forall \delta \boldsymbol{u}^{\mathrm{M}} \in \mathbb{U}^{\mathrm{M},0}, \tag{9}$$

$$\int_{A} \langle \boldsymbol{\sigma}(\boldsymbol{\epsilon}[\boldsymbol{u}^{\mathrm{M}} + \boldsymbol{u}^{\mathrm{s}}]) : \boldsymbol{\epsilon}[\delta \boldsymbol{u}^{\mathrm{s}}] \rangle_{\square} \mathrm{d}A = \int_{A} \langle \boldsymbol{t}_{\mathrm{p}} \cdot \delta \boldsymbol{u}^{\mathrm{s}} \rangle_{\square}^{\gamma} \mathrm{d}A \quad \forall \delta \boldsymbol{u}^{\mathrm{s}} \in \mathbb{U}^{\mathrm{s}}. \tag{10}$$

Here, Eq. (9) constitutes the macro-scale problem, while Eq. (10) defines the sub-scale problem.

2.4. Prolongation and homogenisation

In this section we will define the coupling between the macro-scale fields and the resolved fields within each SVE, via a set of prolongation and homogenisation conditions. In the following, variables with a hat, $\hat{\bullet}$, represents quantities on the mid-surface of the plate, while variables with a bar, $\bar{\bullet}$, represents macro-scopic (and thereby also homogenised) quantities. Furthermore, we introduce the in-plane projection operator $\hat{\boldsymbol{I}} = \boldsymbol{e}_1 \otimes \boldsymbol{e}_1 + \boldsymbol{e}_2 \otimes \boldsymbol{e}_2$.

For the shell kinematics on the macro-scale, we adopt a classic Reissner-Mindlin shell theory. Here, the displacement at a macro-scopic coordinate $\boldsymbol{x} = x_1 \boldsymbol{e}_1 + x_2 \boldsymbol{e}_2 + z \boldsymbol{e}_3$ (in the reference body) can be expressed with five fields defined at each mid-surface coordinate $\hat{\boldsymbol{x}} = \hat{\boldsymbol{I}} \cdot \boldsymbol{x} = x_1 \boldsymbol{e}_1 + x_2 \boldsymbol{e}_2$:

$$\boldsymbol{u}^{\mathrm{RM}}(\hat{\boldsymbol{x}}, z) = \bar{u}_1(\hat{\boldsymbol{x}}) \boldsymbol{e}_1 + \bar{u}_2(\hat{\boldsymbol{x}}) \boldsymbol{e}_2 - z \bar{\theta}_1(\hat{\boldsymbol{x}}) \boldsymbol{e}_1 - z \bar{\theta}_2(\hat{\boldsymbol{x}}) \boldsymbol{e}_2 + \bar{w}(\hat{\boldsymbol{x}}) \boldsymbol{e}_3 \tag{11}$$

where $\bar{u}_1(\hat{\boldsymbol{x}})$, $\bar{u}_2(\hat{\boldsymbol{x}})$ and $\bar{w}(\hat{\boldsymbol{x}})$ represent the displacement of the mid-surface, and $\bar{\theta}_1(\hat{\boldsymbol{x}})$ and $\bar{\theta}_2(\hat{\boldsymbol{x}})$ are fields describing the rotation of through-thickness cross-sections. This can be expressed in a slightly more compact format as:

$$\boldsymbol{u}^{\mathrm{RM}}(\hat{\boldsymbol{x}}, z) = \bar{\boldsymbol{u}}(\hat{\boldsymbol{x}}) - z \bar{\boldsymbol{\theta}}(\hat{\boldsymbol{x}}) + \bar{w}(\hat{\boldsymbol{x}}) \boldsymbol{e}_3, \tag{12}$$

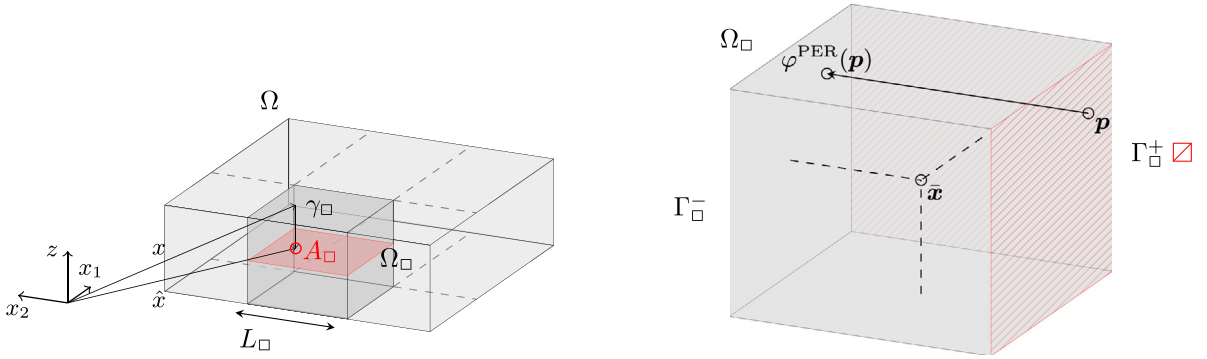

Fig. 3. (a) A volume element embedded in the macro-scopic plate, and (b) illustration of the periodic mapping $\boldsymbol{\varphi}^{\mathrm{PER}} : \Gamma_{\square}^{+} \to \Gamma_{\square}^{-}$. Note that the volume element is depicted as a cube, but could take the shape of any periodic structure.

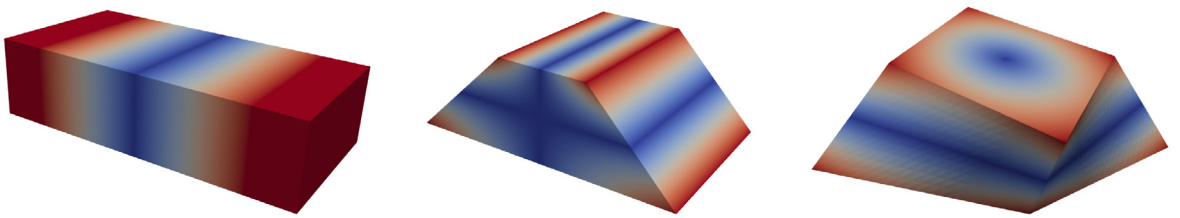

(a) $\varepsilon_{11} = 1.0$ (b) $\kappa_{11} = 1.0$ (c) $\kappa_{12} = \kappa_{21} = 1.0$

Fig. 4. Visualisation of elongation, bending and symmetric twisting deformations from $\boldsymbol{u}^{\mathrm{M}}$. The colours show the normalised magnitude of the deformation.

where we have introduced

$$\bar{\boldsymbol{u}}(\hat{\boldsymbol{x}}) = \bar{u}_1(\hat{\boldsymbol{x}})\boldsymbol{e}_1 + \bar{u}_2(\hat{\boldsymbol{x}})\boldsymbol{e}_2, \qquad \bar{\boldsymbol{\theta}}(\hat{\boldsymbol{x}}) = \bar{\theta}_1(\hat{\boldsymbol{x}})\boldsymbol{e}_1 + \bar{\theta}_2(\hat{\boldsymbol{x}})\boldsymbol{e}_2. \tag{13}$$

Next, we introduce the prolongation operator $\boldsymbol{\mathcal{A}} : \{\bar{u}_1, \bar{u}_2, \bar{w}, \bar{\theta}_1, \bar{\theta}_2\} \to \boldsymbol{u}^{\mathrm{M}}$, which prolongs the macro-scopic fields to the SVE. It is obtained in the spirit of first order homogenisation, where we perform a first order Taylor expansion of $\boldsymbol{u}^{\mathrm{RM}}$ in the in-plane direction, around a point corresponding to the centroid of the SVE, $\bar{\boldsymbol{x}} = \bar{x}_1\boldsymbol{e}_1 + \bar{x}_2\boldsymbol{e}_2$:

$$\begin{aligned} \boldsymbol{u}^{\mathrm{M}}(\hat{\boldsymbol{x}}, z) &= \boldsymbol{u}^{\mathrm{RM}}(\bar{\boldsymbol{x}}, z) + (\boldsymbol{u}^{\mathrm{RM}} \otimes \hat{\boldsymbol{\nabla}})\big|_{\hat{\boldsymbol{x}}=\bar{\boldsymbol{x}}} \cdot \big[\hat{\boldsymbol{x}} - \bar{\boldsymbol{x}}\big] \\ &= \bar{\boldsymbol{u}}(\bar{\boldsymbol{x}}) + \bar{\boldsymbol{h}}(\bar{\boldsymbol{x}}) \cdot [\hat{\boldsymbol{x}} - \bar{\boldsymbol{x}}] - z\bar{\boldsymbol{\theta}}(\bar{\boldsymbol{x}}) - z\bar{\boldsymbol{\kappa}}(\bar{\boldsymbol{x}}) \cdot [\hat{\boldsymbol{x}} - \bar{\boldsymbol{x}}] + \bar{w}(\bar{\boldsymbol{x}})\boldsymbol{e}_3 + \bar{\boldsymbol{g}}(\bar{\boldsymbol{x}}) \cdot [\hat{\boldsymbol{x}} - \bar{\boldsymbol{x}}]\boldsymbol{e}_3 \quad \text{in } \Omega_{\square}, \end{aligned} \tag{14}$$

where $\hat{\boldsymbol{\nabla}} = \hat{\boldsymbol{I}} \cdot \boldsymbol{\nabla} = \boldsymbol{e}_1 \frac{\partial}{\partial x_1} + \boldsymbol{e}_2 \frac{\partial}{\partial x_2}$, and the following gradients have been defined:

$$\bar{\boldsymbol{h}}(\bar{\boldsymbol{x}}) = (\bar{\boldsymbol{u}}(\hat{\boldsymbol{x}}) \otimes \hat{\boldsymbol{\nabla}})\big|_{\hat{\boldsymbol{x}}=\bar{\boldsymbol{x}}}, \qquad \bar{\boldsymbol{\kappa}}(\bar{\boldsymbol{x}}) = (\bar{\boldsymbol{\theta}}(\hat{\boldsymbol{x}}) \otimes \hat{\boldsymbol{\nabla}})\big|_{\hat{\boldsymbol{x}}=\bar{\boldsymbol{x}}}, \qquad \bar{\boldsymbol{g}}(\bar{\boldsymbol{x}}) = \hat{\boldsymbol{\nabla}}\bar{w}(\hat{\boldsymbol{x}})\big|_{\hat{\boldsymbol{x}}=\bar{\boldsymbol{x}}}. \tag{15}$$

As an illustration, the prolongations of macro-scopic elongation ($\varepsilon_{11} = 1.0$), bending ($\kappa_{11} = 1.0$) and symmetric twisting ($\kappa_{12} = \kappa_{21} = 1.0$) for a rectangular SVE are visualised in Fig. 4.

Next, we need to define the homogenisation operators for the five macro-scopic fields and their gradients, $\boldsymbol{\mathcal{A}}^* : \boldsymbol{u} \to \{\bar{u}_1, \bar{u}_2, \bar{w}, \bar{\theta}_1, \bar{\theta}_2\}$. For consistency, the homogenisation of the sub-structural deformation, $\boldsymbol{u}$, should return the macro-scopic field variables, i.e.:

$$\begin{aligned} &\bar{\boldsymbol{u}}_{\square}(\boldsymbol{u}) = \bar{\boldsymbol{u}}, \quad \bar{\boldsymbol{\theta}}_{\square}(\boldsymbol{u}) = \bar{\boldsymbol{\theta}}, \quad \bar{w}_{\square}(\boldsymbol{u}) = \bar{w}, \\ &\bar{\boldsymbol{h}}_{\square}(\boldsymbol{u}) = \bar{\boldsymbol{h}}, \quad \bar{\boldsymbol{\kappa}}_{\square}(\boldsymbol{u}) = \bar{\boldsymbol{\kappa}}, \quad \bar{\boldsymbol{g}}_{\square}(\boldsymbol{u}) = \bar{\boldsymbol{g}}, \end{aligned} \tag{16}$$

where $(\bullet)_{\square}$ denotes the homogenisation operators and where we have (for readability) dropped the implicit dependence of $\bar{\boldsymbol{x}}$ of the macro-scopic fields. Furthermore, as discussed in [17], in order to have a unique

decomposition of $\boldsymbol{u}^{\mathrm{M}}$ and $\boldsymbol{u}^{\mathrm{s}}$ (cf. Eq. (4)), the homogenisation operators should fulfil the following requirements:

$$\begin{aligned} &\bar{\boldsymbol{u}}_{\square}(\boldsymbol{u}^{\mathrm{M}}) = \bar{\boldsymbol{u}}, \quad \bar{\boldsymbol{\theta}}_{\square}(\boldsymbol{u}^{\mathrm{M}}) = \bar{\boldsymbol{\theta}}, \quad \bar{w}_{\square}(\boldsymbol{u}^{\mathrm{M}}) = \bar{w}, \\ &\bar{\boldsymbol{h}}_{\square}(\boldsymbol{u}^{\mathrm{M}}) = \bar{\boldsymbol{h}}, \quad \bar{\boldsymbol{\kappa}}_{\square}(\boldsymbol{u}^{\mathrm{M}}) = \bar{\boldsymbol{\kappa}}, \quad \bar{\boldsymbol{g}}_{\square}(\boldsymbol{u}^{\mathrm{M}}) = \bar{\boldsymbol{g}}, \end{aligned} \tag{17}$$

and

$$\begin{aligned} &\bar{\boldsymbol{u}}_{\square}(\boldsymbol{u}^{\mathrm{s}}) = \boldsymbol{0}, \quad \bar{\boldsymbol{\theta}}_{\square}(\boldsymbol{u}^{\mathrm{s}}) = \boldsymbol{0}, \quad \bar{w}_{\square}(\boldsymbol{u}^{\mathrm{s}}) = 0, \\ &\bar{\boldsymbol{h}}_{\square}(\boldsymbol{u}^{\mathrm{s}}) = \boldsymbol{0}, \quad \bar{\boldsymbol{\kappa}}_{\square}(\boldsymbol{u}^{\mathrm{s}}) = \boldsymbol{0}, \quad \bar{\boldsymbol{g}}_{\square}(\boldsymbol{u}^{\mathrm{s}}) = \boldsymbol{0} \end{aligned} \tag{18}$$

There are different ways of formulating the homogenisation operators such that the requirements in Eq. (17) are fulfilled. For the primary fields, we here make the choice:

$$\bar{\boldsymbol{u}}_{\square}(\boldsymbol{u}) = \frac{1}{|\Omega_{\square}|}\int_{\Omega_{\square}} \hat{\boldsymbol{I}} \cdot \boldsymbol{u}\mathrm{d}\Omega, \tag{19}$$

$$\bar{\boldsymbol{\theta}}_{\square}(\boldsymbol{u}) = -\frac{1}{I_{\square}}\int_{\Omega_{\square}} z\hat{\boldsymbol{I}} \cdot \boldsymbol{u}\mathrm{d}\Omega, \tag{20}$$

$$\bar{w}_{\square}(\boldsymbol{u}) = \frac{1}{|\Omega_{\square}|}\int_{\Omega_{\square}} \boldsymbol{e}_3 \cdot \boldsymbol{u}\mathrm{d}\Omega, \tag{21}$$

where $|\Omega_{\square}| = \int_{\Omega_{\square}} \mathrm{d}\Omega$ and $I_{\square} = \int_{\Omega_{\square}} z^2\mathrm{d}\Omega$. For the homogenisation operators of the gradients of the primary fields, it is convenient to define them as the sensitivities of Eqs. (19)–(21) w.r.t. the placement of the SVE-window. This procedure is explained in detail in Appendix A. For brevity, only the result is give here:

$$\bar{\boldsymbol{h}}_{\square}(\boldsymbol{u}) = \frac{1}{\Omega_{\square}}\int_{\Gamma^{+}_{\square}} \hat{\boldsymbol{I}} \cdot [\![\boldsymbol{u}]\!] \otimes \boldsymbol{n}\mathrm{d}\Gamma, \tag{22}$$

$$\bar{\boldsymbol{\kappa}}_{\square}(\boldsymbol{u}) = -\frac{1}{I_{\square}}\int_{\Gamma^{+}_{\square}} z\hat{\boldsymbol{I}} \cdot [\![\boldsymbol{u}]\!] \otimes \boldsymbol{n}\mathrm{d}\Gamma, \tag{23}$$

$$\bar{\boldsymbol{g}}_{\square}(\boldsymbol{u}) = \frac{1}{\Omega_{\square}}\int_{\Gamma^{+}_{\square}} (\boldsymbol{e}_3 \cdot [\![\boldsymbol{u}]\!])\boldsymbol{n}\mathrm{d}\Gamma. \tag{24}$$

In Eqs. (22)–(24), we have introduced the *image part* of the boundary section $\Gamma^{+}_{\square}$, linked to the complementary *mirror part* $\Gamma^{-}_{\square}$, see Fig. 3(b) for an illustration. Furthermore, we have also introduced the mapping $\boldsymbol{\varphi}^{\mathrm{PER}} : \Gamma^{+}_{\square} \rightarrow \Gamma^{-}_{\square}$ to define the jump operator $[\![\bullet]\!]$:

$$[\![f]\!](\boldsymbol{x}^{+}) = f(\boldsymbol{x}^{+}) - f(\boldsymbol{\varphi}^{\mathrm{PER}}(\boldsymbol{x}^{+})) \quad \text{on} \quad \Gamma^{+}_{\square}. \tag{25}$$

The requirements in Eq. (17) are automatically fulfilled by our choice of homogenisation operators. The requirements in Eq. (18), however, will be satisfied by imposing them as constraints for the SVE-problem, see Section 4 for more details. Finally, the conditions in Eq. (18) together with the prolongation and homogenisation operators satisfying Eq. (17), guarantees kinematically consistency.

3. Macro-scale problem

In this section we will establish the weak form of the macro-scale problem. This is achieved by introducing the prolongation $\boldsymbol{u}^{\mathrm{M}}$ in Eq. (14), into Eq. (9) for the test-functions $\delta\boldsymbol{u}$. Considering the left-hand side, this results in:

$$\begin{aligned} &\int_A \langle \boldsymbol{\sigma}(\boldsymbol{\epsilon}[\boldsymbol{u}^{\mathrm{M}} + \boldsymbol{u}^{\mathrm{s}}]) : \boldsymbol{\epsilon}[\delta\boldsymbol{u}^{\mathrm{M}}]\rangle_{\square}\mathrm{d}A = \\ &\int_A \frac{1}{A_{\square}}\int_{\Omega_{\square}} \boldsymbol{\sigma} : \boldsymbol{\epsilon}[\delta\bar{\boldsymbol{u}} + \delta\bar{\boldsymbol{h}} \cdot [\hat{\boldsymbol{x}} - \bar{\boldsymbol{x}}] - z\delta\bar{\boldsymbol{\theta}} - z\delta\bar{\boldsymbol{\kappa}} \cdot [\hat{\boldsymbol{x}} - \bar{\boldsymbol{x}}] + \delta\bar{w}\boldsymbol{e}_3 + \delta\bar{\boldsymbol{g}} \cdot [\hat{\boldsymbol{x}} - \bar{\boldsymbol{x}}]\boldsymbol{e}_3]\mathrm{d}\Omega\mathrm{d}A. \end{aligned} \tag{26}$$

By considering each term in $\delta\boldsymbol{\epsilon}[\boldsymbol{u}^{\mathrm{M}}]$, and using the fact that the macro-scopic fields are constant within each SVE, the well-known weak form of the Reissner-Mindlin plate equations is obtained:

$$\int_A \langle \boldsymbol{\sigma}(\boldsymbol{\epsilon}[\boldsymbol{u}^{\mathrm{M}} + \boldsymbol{u}^{\mathrm{s}}]) : \boldsymbol{\epsilon}[\delta\boldsymbol{u}^{\mathrm{M}}]\rangle_{\square}\mathrm{d}A = \int_A \bar{\boldsymbol{N}} : \delta\bar{\boldsymbol{h}} + \bar{\boldsymbol{V}} \cdot (\delta\bar{\boldsymbol{g}} - \delta\bar{\boldsymbol{\theta}}) - \bar{\boldsymbol{M}} : \delta\bar{\boldsymbol{\kappa}}\mathrm{d}A. \tag{27}$$

Here, the SVE problem acts as the constitutive relation for the normal forces, $\bar{\boldsymbol{N}}$, shear forces, $\bar{\boldsymbol{V}}$, and bending moments $\bar{\boldsymbol{M}}$:

$$\bar{\boldsymbol{N}} = \frac{1}{A_\square}\int_{\Omega_\square} \hat{\boldsymbol{I}}\cdot\boldsymbol{\sigma}\cdot\hat{\boldsymbol{I}}\,\mathrm{d}\Omega, \tag{28}$$

$$\bar{\boldsymbol{V}} = \frac{1}{A_\square}\int_{\Omega_\square} \hat{\boldsymbol{I}}\cdot\boldsymbol{\sigma}\cdot\boldsymbol{e}_3\,\mathrm{d}\Omega, \tag{29}$$

$$\bar{\boldsymbol{M}} = \frac{1}{A_\square}\int_{\Omega_\square} z\left(\hat{\boldsymbol{I}}\cdot\boldsymbol{\sigma}\cdot\hat{\boldsymbol{I}}\right) + (\hat{\boldsymbol{I}}\cdot\boldsymbol{\sigma}\cdot\boldsymbol{e}_3)\otimes(\hat{\boldsymbol{x}}-\bar{\boldsymbol{x}})\,\mathrm{d}\Omega. \tag{30}$$

Next, we consider the first term on the right-hand side of Eq. (9), which is expressed as:

$$\int_A \langle \boldsymbol{t}_\mathrm{p}\cdot\delta\boldsymbol{u}^\mathrm{M}\rangle_\square^\gamma \mathrm{d}A = \int_A \bar{\boldsymbol{q}}^u\cdot\delta\bar{\boldsymbol{u}}\,\mathrm{d}\Gamma + \int_A \bar{\boldsymbol{q}}^h : \delta\bar{\boldsymbol{h}}\,\mathrm{d}\Gamma + \int_A \bar{q}^w\delta\bar{w}\,\mathrm{d}\Gamma + \int_A \bar{\boldsymbol{q}}^g\cdot\delta\bar{\boldsymbol{g}}\,\mathrm{d}\Gamma - \int_A \bar{\boldsymbol{q}}^\theta\cdot\delta\bar{\boldsymbol{\theta}}\,\mathrm{d}\Gamma - \int_A \bar{\boldsymbol{q}}^\kappa : \delta\bar{\boldsymbol{\kappa}}\,\mathrm{d}\Gamma \tag{31}$$

where the loading terms are defined as:

$$\bar{\boldsymbol{q}}^u = \frac{1}{A_\square}\int_{\gamma_\square} \hat{\boldsymbol{I}}\cdot\boldsymbol{t}_p\,\mathrm{d}\Gamma, \qquad \bar{\boldsymbol{q}}^\theta = \frac{1}{A_\square}\int_{\gamma_\square} z\hat{\boldsymbol{I}}\cdot\boldsymbol{t}_p\,\mathrm{d}\Gamma, \quad \bar{q}^w = \frac{1}{A_\square}\int_{\gamma_\square} \boldsymbol{e}_3\cdot\boldsymbol{t}_p\,\mathrm{d}\Gamma \tag{32}$$

$$\bar{\boldsymbol{q}}^h = \frac{1}{A_\square}\int_{\gamma_\square} \hat{\boldsymbol{I}}\cdot\boldsymbol{t}_p\otimes(\hat{\boldsymbol{x}}-\bar{\boldsymbol{x}})\,\mathrm{d}\Gamma, \qquad \bar{\boldsymbol{q}}^\kappa = \frac{1}{A_\square}\int_{\gamma_\square} z\hat{\boldsymbol{I}}\cdot\boldsymbol{t}_p\otimes(\hat{\boldsymbol{x}}-\bar{\boldsymbol{x}})\,\mathrm{d}\Gamma, \quad \bar{\boldsymbol{q}}^g = \frac{1}{A_\square}\int_{\gamma_\square} \boldsymbol{e}_3\cdot\boldsymbol{t}_p\otimes(\hat{\boldsymbol{x}}-\bar{\boldsymbol{x}})\,\mathrm{d}\Gamma. \tag{33}$$

Finally, considering the second term on the right-hand side of Eq. (9), i.e. the term containing boundary conditions on Γ, we will assume Reissner-Mindlin kinematics (cf. Eq. (11)):

$$\int_\Gamma \boldsymbol{t}_p\cdot\delta\boldsymbol{u}^\mathrm{M}\,\mathrm{d}\Gamma = \int_\Gamma \hat{\boldsymbol{I}}\cdot\boldsymbol{t}_p\cdot\delta\bar{\boldsymbol{u}}\,\mathrm{d}\Gamma + \int_\Gamma (\boldsymbol{e}_3\cdot\boldsymbol{t}_p)\delta\bar{w}\,\mathrm{d}\Gamma - \int_\Gamma z\hat{\boldsymbol{I}}\cdot\boldsymbol{t}_p\cdot\delta\bar{\boldsymbol{\theta}}\,\mathrm{d}\Gamma. \tag{34}$$

For Dirichlet boundary conditions on Γ, we simply restrict the test and trial spaces to

$$\begin{aligned}
&\bar{\mathbb{U}}_u = \{\boldsymbol{v}\in[\mathbb{H}^1(A)]^2 \quad | \quad \boldsymbol{v}=\boldsymbol{u}^p \text{ on } \Gamma_{D,u}\}, \quad \bar{\mathbb{U}}_u^0 = \{\boldsymbol{v}\in[\mathbb{H}^1(A)]^2 \quad | \quad \boldsymbol{v}=\boldsymbol{0} \text{ on } \Gamma_{D,u}\},\\
&\bar{\mathbb{U}}_\theta = \{\boldsymbol{v}\in[\mathbb{H}^1(A)]^2 \quad | \quad \boldsymbol{v}=\boldsymbol{\theta}^p \text{ on } \Gamma_{D,\theta}\}, \quad \bar{\mathbb{U}}_\theta^0 = \{\boldsymbol{v}\in[\mathbb{H}^1(A)]^2 \quad | \quad \boldsymbol{v}=\boldsymbol{0} \text{ on } \Gamma_{D,\theta}\},\\
&\bar{\mathbb{U}}_w = \{v\in\mathbb{H}^1(A) \quad | \quad v=w^p \text{ on } \Gamma_{D,w}\}, \quad \bar{\mathbb{U}}_w^0 = \{v\in\mathbb{H}^1(A) \quad | \quad v=0 \text{ on } \Gamma_{D,w}\}.
\end{aligned} \tag{35}$$

With the reformulation of the left- and right-hand side right of Eq. (9), the macro-scale problem can now be stated as finding $\bar{\boldsymbol{u}}\in\bar{\mathbb{U}}_u$, $\bar{w}\in\bar{\mathbb{U}}_w$, $\bar{\boldsymbol{\theta}}\in\bar{\mathbb{U}}_\theta$ such that:

$$\int_A \bar{\boldsymbol{N}} : \delta\bar{\boldsymbol{h}}\,\mathrm{d}A = \int_A \bar{\boldsymbol{q}}^u\cdot\delta\bar{\boldsymbol{u}}\,\mathrm{d}\Gamma + \int_A \bar{\boldsymbol{q}}^h : \delta\bar{\boldsymbol{h}}\,\mathrm{d}\Gamma + \int_\Gamma \boldsymbol{t}_p\cdot\delta\bar{\boldsymbol{u}} \quad \forall\delta\bar{\boldsymbol{u}}\in\bar{\mathbb{U}}_u^0, \tag{36}$$

$$\int_A \bar{\boldsymbol{V}}\cdot\delta\bar{\boldsymbol{g}}\,\mathrm{d}A = \int_A \bar{q}^w\delta\bar{w}\,\mathrm{d}\Gamma + \int_A \bar{\boldsymbol{q}}^g\cdot\delta\bar{\boldsymbol{g}}\,\mathrm{d}\Gamma + \int_\Gamma (\boldsymbol{e}_3\cdot\boldsymbol{t}_p)\delta\bar{w}\,\mathrm{d}\Gamma \quad \forall\delta\bar{w}\in\bar{\mathbb{U}}_w^0, \tag{37}$$

$$\int_A \bar{\boldsymbol{V}}\cdot\delta\bar{\boldsymbol{\theta}} + \bar{\boldsymbol{M}} : \delta\bar{\boldsymbol{\kappa}}\,\mathrm{d}A = \int_A \bar{\boldsymbol{q}}^\theta\cdot\delta\bar{\boldsymbol{\theta}}\,\mathrm{d}\Gamma + \int_A \bar{\boldsymbol{q}}^\kappa : \delta\bar{\boldsymbol{\kappa}}\,\mathrm{d}\Gamma + \int_\Gamma z\boldsymbol{t}_p\cdot\delta\bar{\boldsymbol{\theta}}\,\mathrm{d}\Gamma \quad \forall\delta\bar{\boldsymbol{\theta}}\in\bar{\mathbb{U}}_\theta^0. \tag{38}$$

Note that Eqs. (36)–(38) resemble the weak form of the classical Reissner-Mindlin plate equations, with the exception that the membrane, bending and shear forces are obtained from the SVE-problem.

4. The SVE problem

In this section, the boundary value problem for sub-scale problem, defined by Eq. (10), will be established in terms of the unknown fluctuation field $\boldsymbol{u}^\mathrm{s}$.

As a first step towards establishing the SVE-problem, we will assume that the SVE-volumes are independent of each other, i.e. we perform a local approximation (as described in Eq. (10)) for each SVE-volume $\Omega_\square$. As such, the governing equation for the boundary value problem for the SVE becomes:

$$\frac{1}{A_\square}\int_{\Omega_\square} \boldsymbol{\sigma}(\boldsymbol{\epsilon}[\boldsymbol{u}^\mathrm{M}+\boldsymbol{u}^\mathrm{s}]) : \boldsymbol{\epsilon}[\delta\boldsymbol{u}^\mathrm{s}]\,\mathrm{d}\Omega = \frac{1}{A_\square}\int_{\gamma_\square} \boldsymbol{t}_\mathrm{p}\cdot\delta\boldsymbol{u}^\mathrm{s}\,\mathrm{d}\Gamma \quad \forall\delta\boldsymbol{u}^\mathrm{s}\in\mathbb{U}_\square^\mathrm{s}. \tag{39}$$

Remark. Note that the deformation measures on the macro-scale, i.e. $\bar{\boldsymbol{h}}$, $\bar{\boldsymbol{\kappa}}$, $\bar{\boldsymbol{\theta}}$ and $\bar{\boldsymbol{g}}$, enters the SVE-problem via the term $\boldsymbol{\epsilon}(\boldsymbol{u}^M)$. On closer inspection, we can identify that $\boldsymbol{\epsilon}(\boldsymbol{u}^M)$ can be written as:

$$\boldsymbol{\epsilon}(\boldsymbol{u}^M) = \bar{\boldsymbol{\varepsilon}} - (z\hat{\boldsymbol{\mathcal{I}}}^{\text{sym}} - \boldsymbol{\mathcal{I}}_3 \otimes (\hat{\boldsymbol{x}} - \bar{\boldsymbol{x}})) : \bar{\boldsymbol{\kappa}} + \boldsymbol{\mathcal{I}}_3 \cdot \bar{\boldsymbol{\gamma}} \tag{40}$$

where

$$\boldsymbol{\mathcal{I}}_3 = \sum_{\alpha=1}^{3} [\boldsymbol{e}_3 \otimes \boldsymbol{e}_\alpha] \otimes \boldsymbol{e}_\alpha, \qquad \hat{\boldsymbol{\mathcal{I}}}^{\text{sym}} = \frac{1}{2}(\hat{\boldsymbol{I}} \overline{\otimes} \hat{\boldsymbol{I}} + \hat{\boldsymbol{I}} \underline{\otimes} \hat{\boldsymbol{I}}) \tag{41}$$

and where we have introduced the measures

$$\bar{\boldsymbol{\varepsilon}} = \bar{\boldsymbol{h}}^{\text{sym}}, \qquad \bar{\boldsymbol{\gamma}} = \bar{\boldsymbol{g}} - \bar{\boldsymbol{\theta}}. \tag{42}$$

Thus, the SVE-problem is invariant to the terms $\bar{\boldsymbol{g}} + \bar{\boldsymbol{\theta}}$ and $\bar{\boldsymbol{h}}^{\text{skw}}$, and the sectional forces $\bar{\boldsymbol{N}}$, $\bar{\boldsymbol{M}}$ and $\bar{\boldsymbol{V}}$ are implicit functions of $\bar{\boldsymbol{\varepsilon}}$, $\bar{\boldsymbol{\kappa}}$ and $\bar{\boldsymbol{\gamma}}$. □

Next, as discussed in Section 2.4, we require that the homogenised measures vanishes for the fluctuations $\boldsymbol{u}^{\text{s}}$ in order to ensure a proper decomposition of $\boldsymbol{u} = \boldsymbol{u}^{\text{M}} + \boldsymbol{u}^{\text{s}}$. This amounts to enforcing the constraints:

$$\bar{\boldsymbol{u}}_\square(\boldsymbol{u}^{\text{s}}) = \boldsymbol{0} \tag{43}$$

$$\bar{w}_\square(\boldsymbol{u}^{\text{s}}) = 0 \tag{44}$$

$$\bar{\boldsymbol{\theta}}_\square(\boldsymbol{u}^{\text{s}}) = \boldsymbol{0} \tag{45}$$

$$\bar{\boldsymbol{h}}_\square(\boldsymbol{u}^{\text{s}}) = \boldsymbol{0} \tag{46}$$

$$\bar{\boldsymbol{g}}_\square(\boldsymbol{u}^{\text{s}}) = \boldsymbol{0} \tag{47}$$

$$\bar{\boldsymbol{\kappa}}_\square(\boldsymbol{u}^{\text{s}}) = \boldsymbol{0} \tag{48}$$

Eqs. (43) and (44) simply constrain any rigid body translation of the SVE. In practice, these can be enforced by simply locking a single node on the SVE mesh, or in the presence of a net force contribution from $\boldsymbol{t}_{\text{p}}$, by enforcing the constraints weakly (via Lagrange multipliers). Eqs. (46)–(48) constrains the fluctuation fields on the lateral faces of the SVE. As will be shown in the next section, these constraints can be automatically fulfilled by the boundary conditions that are introduced in Sections 4.1–4.4. Finally, and most interestingly, the constraints in Eqs. (45), here written out explicitly,

$$\bar{\theta}_{1,\square} = \int_{\Omega_\square} z\boldsymbol{e}_1 \cdot \boldsymbol{u} \mathrm{d}\Omega = 0, \qquad \bar{\theta}_{2,\square} = \int_{\Omega_\square} z\boldsymbol{e}_2 \cdot \boldsymbol{u} \mathrm{d}\Omega = 0, \tag{49}$$

enforces the volume averaged transverse shear angles of the SVE to be equal to the macro-scopic counter-part. These constraints will counteract any coupled bending-shear behaviour of the SVE, when subjected to transverse shear loads. Interestingly, these are essentially the same constraints as those proposed by Hii et al. [9], although here they follow naturally from the VCH approach rather than being partially postulated.

As a last step towards formulating the boundary value problem for the SVE, boundary conditions on the sub-scale fluctuations needs to be specified. In this work, we will consider boundary conditions of three different types: *(i)* periodic, *(ii)* Dirichlet, and *(iii)* Neumann. Periodic boundary conditions are typically considered the best choice in practical applications even when the subscale geometry is not periodic. However, Dirichlet and Neumann boundary conditions may be useful for obtaining upper and lower bounds of the solution.

In the following subsections, different versions of the mentioned boundary conditions are discussed and the corresponding boundary value problems are established.

4.1. Periodic boundary conditions

The periodic boundary conditions for the fluctuation field can be stated as:

$$[\![\boldsymbol{u}^{\text{s}}]\!] = \boldsymbol{0} \quad \text{on} \quad \Gamma_\square^+. \tag{50}$$

These constraints can either be enforced weakly using Lagrange multipliers, or with the use of linear constraints if $\Gamma_\square^+$ and $\Gamma_\square^-$ have matching discretisations. Furthermore, it can be verified that this boundary condition automatically fulfils Eqs. (46)–(48).

Moreover, the two volume constraints in Eq. (45) are enforced with Lagrange multipliers $\boldsymbol{\lambda}_\theta$. The micro-periodic SVE-problem can thus be stated as that of finding $\boldsymbol{u}^{\mathrm{s}}, \boldsymbol{\lambda}_\theta \in \mathbb{U}_\square^{\mathrm{PBC}} \times \mathbb{R}^2$ such that:

$$\begin{aligned} \frac{1}{A_\square}\int_{\Omega_\square} \boldsymbol{\sigma}(\boldsymbol{\epsilon}[\boldsymbol{u}^{\mathrm{M}}+\boldsymbol{u}^{\mathrm{s}}]) : \boldsymbol{\epsilon}[\delta\boldsymbol{u}^{\mathrm{s}}]\mathrm{d}\Omega + \boldsymbol{\lambda}_\theta \cdot \bar{\boldsymbol{\theta}}_\square(\delta\boldsymbol{u}^{\mathrm{s}}) = \frac{1}{A_\square}\int_{\gamma_\square} \boldsymbol{t}_{\mathrm{p}} \cdot \delta\boldsymbol{u}^{\mathrm{s}}\mathrm{d}\Gamma \quad \forall \delta\boldsymbol{u}^{\mathrm{s}} \in \mathbb{U}_\square^{\mathrm{PBC}}, \\ \delta\boldsymbol{\lambda}_\theta \cdot \bar{\boldsymbol{\theta}}_\square(\boldsymbol{u}^{\mathrm{s}}) = 0 \quad \forall \delta\boldsymbol{\lambda}_\theta \in \mathbb{R}^2, \end{aligned} \tag{51}$$

where

$$\mathbb{U}_\square^{\mathrm{PBC}} = \{\boldsymbol{v} \in [\mathbb{H}^1(\Omega_\square)]^2 : [\![\boldsymbol{v}]\!] = \boldsymbol{0} \text{ on } \Gamma_\square^+, \int_{\Omega_\square} \boldsymbol{v}\mathrm{d}\Omega = 0\}. \tag{52}$$

Here, the rigid body translations in Eqs. (43)–(44) are formally included in $\mathbb{U}_\square^{\mathrm{PBC}}$. In the case that $\boldsymbol{t}_p$ does not exert a net force on the SVE, this constraint can simply be replaced by locking one arbitrary node in the discrete (FE) problem.

Remark. Periodic boundary conditions are typically applied to SVEs with periodic geometries. However, in the context of the framework presented herein, periodic boundary conditions are simply utilised in order to fulfil Eqs. (46)–(48), and can thus be used for geometrically non-periodic SVEs as well (with the assumption that there are no voids on the boundaries). This fact is used in e.g. the numerical example in Section 5.3. □

4.2. Enriched periodic boundary conditions

An SVE-problem modelled with standard periodic boundary conditions is, within the current framework, not able to accurately capture the torsional stiffness in the case of SVEs with large in-plane dimensions. This issue will be demonstrated in Section 5 (numerical examples), but can also be made evident by studying the prolonged macro-scale torsional deformation in Fig. 4(c). In particular, a shortcoming in the macro-scopic prolongation can be noted, as it lacks an anti-periodic twisting mode in the out-of-plane direction. This shortcoming, together with the fact that periodic boundary conditions prevents anti-periodic deformations, means that the torsional stiffness is poorly predicted for SVEs with finite in-plane dimensions.

To avoid an inaccurate prediction of torsional stiffness for the micro-periodic SVE problem, we provide two remedies. The first solution is to improve the prolongation $\boldsymbol{u}^{\mathrm{M}}$ by adding higher order deformation modes that can represent twisting. This approach is presented in Appendix B. The second remedy, which is to be presented in the current subsection, amounts to enriching the fluctuation field $\boldsymbol{u}^{\mathrm{s}}$ with an additional anti-periodic twisting mode. As such, $\boldsymbol{u}^{\mathrm{s}}$ is split into two parts:

$$\boldsymbol{u}^{\mathrm{s}} = \boldsymbol{u}^{\mathrm{s,P}} + \boldsymbol{u}^{\mathrm{s},\xi} \tag{53}$$

where $\boldsymbol{u}^{\mathrm{s,P}}$ is the standard fluctuation field with periodic boundary conditions, i.e. $\boldsymbol{u}^{\mathrm{s,P}} \in \mathbb{U}_\square^{\mathrm{PBC}}$, and $\boldsymbol{u}^{\mathrm{s},\xi}$ is an added anti-periodic fluctuation field which accounts for twisting deformations. Here we propose the field to be defined as:

$$\boldsymbol{u}^{\mathrm{s},\xi} = \frac{1}{2}\left([\hat{\boldsymbol{x}}-\bar{\boldsymbol{x}}]\cdot\boldsymbol{\kappa}_\xi\cdot[\hat{\boldsymbol{x}}-\bar{\boldsymbol{x}}]\right)\boldsymbol{e}_3 - \frac{1}{2}\langle[\hat{\boldsymbol{x}}-\bar{\boldsymbol{x}}]\cdot\boldsymbol{\kappa}_\xi\cdot[\hat{\boldsymbol{x}}-\bar{\boldsymbol{x}}]\rangle_\square\boldsymbol{e}_3 \quad \text{in } \Omega_\square, \tag{54}$$

where $\boldsymbol{\kappa}_\xi \in \mathbb{R}^{2\times 2,sym}$ is an additional unknown symmetric second order tensor. As a consequence of the enrichment of the fluctuation field, three additional global degrees of freedom (to the SVE-problem) are added and need to be solved for. Moreover, due to the proposed form of the enrichment field $\boldsymbol{u}^{\mathrm{s},\xi}$, the homogenisation conditions in Eqs. (46)–(48) are still fulfilled.

The SVE-problem with enriched periodic boundary conditions can be stated as that of finding $\boldsymbol{u}^{\mathrm{s},P}, \boldsymbol{\kappa}_\xi, \boldsymbol{\lambda}_\theta \in \mathbb{U}_\square^{\mathrm{PBC}} \times \mathbb{R}^{2\times 2,sym} \times \mathbb{R}^2$ such that:

$$\begin{aligned} \frac{1}{A_\square}\int_{\Omega_\square} \boldsymbol{\sigma} : \boldsymbol{\epsilon}[\delta\boldsymbol{u}^{\mathrm{s,P}}]\mathrm{d}\Omega + \boldsymbol{\lambda}_\theta \cdot \bar{\boldsymbol{\theta}}_\square(\delta\boldsymbol{u}^{\mathrm{s,P}}) = \frac{1}{A_\square}\int_{\gamma_\square} \boldsymbol{t}_{\mathrm{p}} \cdot \delta\boldsymbol{u}^{\mathrm{s,P}}\mathrm{d}\Gamma \quad \forall \delta\boldsymbol{u}^{\mathrm{s,P}} \in \mathbb{U}_\square^{\mathrm{PBC}}, \\ \frac{1}{A_\square}\int_{\Omega_\square} \boldsymbol{\sigma} : \boldsymbol{\epsilon}[\delta\boldsymbol{u}^{\mathrm{s},\xi}]\mathrm{d}\Omega = \frac{1}{A_\square}\int_{\gamma_\square} \boldsymbol{t}_{\mathrm{p}} \cdot \delta\boldsymbol{u}^{\mathrm{s},\xi}\mathrm{d}\Gamma \quad \forall \delta\boldsymbol{u}^{\mathrm{s},\xi} \in \mathbb{U}_\square^{\xi}, \\ \delta\boldsymbol{\lambda}_\theta \cdot \bar{\boldsymbol{\theta}}_\square(\boldsymbol{u}^{\mathrm{s,P}}) = 0 \quad \forall \delta\boldsymbol{\lambda}_\theta \in \mathbb{R}^2, \end{aligned} \tag{55}$$

where the new space introduced for the enriched fluctuation field is defined as:

$$\mathbb{U}^{\xi}_{\square} = \{\boldsymbol{v} = \frac{1}{2}\left([\hat{\boldsymbol{x}} - \bar{\boldsymbol{x}}] \cdot \boldsymbol{\kappa}_{\xi} \cdot [\hat{\boldsymbol{x}} - \bar{\boldsymbol{x}}]\right)\boldsymbol{e}_3 - \frac{1}{2}\langle [\hat{\boldsymbol{x}} - \bar{\boldsymbol{x}}] \cdot \boldsymbol{\kappa}_{\xi} \cdot [\hat{\boldsymbol{x}} - \bar{\boldsymbol{x}}]\rangle_{\square}\boldsymbol{e}_3, \quad \boldsymbol{\kappa}_{\xi} \in \mathbb{R}^{2\times 2, sym}\}. \tag{56}$$

4.3. Dirichlet boundary conditions

Dirichlet boundary conditions can be expressed as:

$$\boldsymbol{u}^{\mathrm{s}} = \boldsymbol{0} \quad \text{on} \quad \Gamma_{\square}. \tag{57}$$

Similarly to the case with periodic boundary conditions, it can be verified that Eqs. (57) fulfils Eqs. (46)–(48). The rigid body constraints in Eqs. (43) and (44) can be omitted since any rigid body translations are clearly prevented by Eq. (57). The SVE-problem with Dirichlet boundary conditions can thus be stated as that of finding $\boldsymbol{u}^{\mathrm{s}}, \boldsymbol{\lambda}_{\theta} \in \mathbb{U}^{\mathrm{DBC}}_{\square} \times \mathbb{R}^2$ such that:

$$\begin{aligned} \frac{1}{A_{\square}}\int_{\Omega_{\square}} \boldsymbol{\sigma}(\boldsymbol{\epsilon}[\boldsymbol{u}^{\mathrm{M}} + \boldsymbol{u}^{\mathrm{s}}]) : \boldsymbol{\epsilon}[\delta\boldsymbol{u}^{\mathrm{s}}]\mathrm{d}\Omega + \boldsymbol{\lambda}_{\theta} \cdot \bar{\boldsymbol{\theta}}_{\square}(\delta\boldsymbol{u}^{\mathrm{s}}) = \frac{1}{A_{\square}}\int_{\gamma_{\square}} \boldsymbol{t}_{\mathrm{p}} \cdot \delta\boldsymbol{u}^{\mathrm{s}}\mathrm{d}\Gamma \quad \forall \delta\boldsymbol{u}^{\mathrm{s}} \in \mathbb{U}^{\mathrm{DBC}}_{\square}, \\ \delta\boldsymbol{\lambda}_{\theta} \cdot \bar{\boldsymbol{\theta}}_{\square}(\boldsymbol{u}^{\mathrm{s}}) = 0 \quad \forall \delta\boldsymbol{\lambda}_{\theta} \in \mathbb{R}^2, \end{aligned} \tag{58}$$

where

$$\mathbb{U}^{\mathrm{DBC}}_{\square} = \{\boldsymbol{v} \in [\mathbb{H}^1(\Omega_{\square})]^2 : \boldsymbol{v} = \boldsymbol{0} \text{ on } \Gamma_{\square}\}. \tag{59}$$

4.4. Relaxed Dirichlet boundary conditions

As will be shown in the section for the numerical results, the Dirichlet boundary condition in Section 4.3 will lead to over-stiff estimations, mostly pronounced in bending. The reason for this is that the Dirichlet condition constrains the z-component of $\boldsymbol{u}^{\mathrm{s}}$ on the lateral faces. As a simple remedy, it is possible to only consider Dirichlet boundary conditions in the in-plane directions:

$$u^{\mathrm{s}}_1 = 0, \quad u^{\mathrm{s}}_2 = 0 \quad \text{on} \quad \Gamma_{\square}, \tag{60}$$

and let the displacement in the out-of-plane direction, u_3, be free. These constraints can be shown to enforce Eq. (46) and (48). However, as u_3 is now free at the lateral boundaries, we need to introduce additional Lagrange multipliers to satisfy Eq. (47). Furthermore, the constraint in Eq. (45) is treated with Lagrange multipliers as before.

In summary, the weak form of the SVE problem with relaxed Dirichlet conditions can be stated as follows: find $\boldsymbol{u}^{\mathrm{s}}, \boldsymbol{\lambda}_{\theta}, \boldsymbol{\lambda}_{g} \in \mathbb{U}^{\mathrm{RDBC}}_{\square} \times \mathbb{R}^2 \times \mathbb{R}^2$ such that:

$$\begin{aligned} \frac{1}{A_{\square}}\int_{\Omega_{\square}} \boldsymbol{\sigma}(\boldsymbol{\epsilon}[\boldsymbol{u}^{\mathrm{M}} + \boldsymbol{u}^{\mathrm{s}}]) : \boldsymbol{\epsilon}[\delta\boldsymbol{u}^{\mathrm{s}}]\mathrm{d}\Omega + \boldsymbol{\lambda}_{\theta} \cdot \bar{\boldsymbol{\theta}}_{\square}(\delta\boldsymbol{u}^{\mathrm{s}}) + \boldsymbol{\lambda}_{g} \cdot \bar{\boldsymbol{g}}_{\square}(\delta\boldsymbol{u}^{\mathrm{s}}) = \frac{1}{A_{\square}}\int_{\gamma_{\square}} \boldsymbol{t}_{\mathrm{p}} \cdot \delta\boldsymbol{u}^{\mathrm{s}}\mathrm{d}\Gamma \quad \forall \delta\boldsymbol{u}^{\mathrm{s}} \in \mathbb{U}^{\mathrm{RDBC}}_{\square}, \\ \delta\boldsymbol{\lambda}_{\theta} \cdot \bar{\boldsymbol{\theta}}_{\square}(\boldsymbol{u}^{\mathrm{s}}) = 0 \quad \forall \delta\boldsymbol{\lambda}_{\theta} \in \mathbb{R}^2, \\ \delta\boldsymbol{\lambda}_{g} \cdot \bar{\boldsymbol{g}}_{\square}(\boldsymbol{u}^{\mathrm{s}}) = 0 \quad \forall \delta\boldsymbol{\lambda}_{g} \in \mathbb{R}^2, \end{aligned} \tag{61}$$

where

$$\mathbb{U}^{\mathrm{RDBC}}_{\square} = \{\boldsymbol{v} \in [\mathbb{H}^1(\Omega_{\square})]^2 : \hat{\boldsymbol{I}} \cdot \boldsymbol{v} = \boldsymbol{0} \text{ on } \Gamma_{\square}, \int_{\Omega_{\square}} \boldsymbol{e}_3 \cdot \boldsymbol{v}\mathrm{d}\Omega = 0\}. \tag{62}$$

We note that the constraint in Eq. (44), formally included in $\mathbb{U}^{\mathrm{RDBC}}_{\square}$, can be enforced by prescribing the vertical displacement of one node in the discrete problem whenever there is no net vertical force or $\boldsymbol{t}_p$.

Remark. As with the case of enriched periodic boundary conditions, it is possible to mitigate the over-stiff behaviour caused by the (standard) Dirichlet conditions, by supplementing the fluctuation field $\boldsymbol{u}^{\mathrm{s}}$ with enriched deformation modes, i.e. one mode that properly accounts for bending and twisting, and another mode that properly accounts for the contraction or expansion in the out-of-plane direction. However, as will be shown in the numerical examples, relaxing the Dirichlet conditions as proposed in this subsection is an alternative remedy that also fits within the overall framework.

4.5. Neumann boundary conditions

The SVE problem with boundary conditions of Neumann type is obtained by enforcing the constraints in Eqs. (45)–(48) with Lagrange parameters. Furthermore, as in Sub- Section 4.1, the rigid-body constraints can be enforced by locking one node in the FE-mesh (in the absence of external net force from $\boldsymbol{t}_p$). The SVE-problem with Neumann boundary conditions can thus be stated as that of finding $\boldsymbol{u}^{\mathrm{s}}, \boldsymbol{\lambda}_\theta, \boldsymbol{\lambda}_h, \boldsymbol{\lambda}_\kappa, \boldsymbol{\lambda}_g \in \mathbb{U}_\square^{\mathrm{NBC}} \times \mathbb{R}^2 \times \mathbb{R}^{2\times 2} \times \mathbb{R}^{2\times 2} \times \mathbb{R}^2$, such that:

$$
\begin{aligned}
\frac{1}{A_\square}\int_{\Omega_\square} \boldsymbol{\sigma}(\boldsymbol{\epsilon}[\boldsymbol{u}^{\mathrm{M}}+\boldsymbol{u}^{\mathrm{s}}]) : \boldsymbol{\epsilon}[\delta\boldsymbol{u}^{\mathrm{s}}]\mathrm{d}\Omega + \boldsymbol{\lambda}_\theta \cdot \bar{\boldsymbol{\theta}}_\square(\delta\boldsymbol{u}^{\mathrm{s}}) + \boldsymbol{\lambda}_h : \bar{\boldsymbol{h}}_\square(\delta\boldsymbol{u}^{\mathrm{s}}) + \boldsymbol{\lambda}_\kappa : \bar{\boldsymbol{\kappa}}_\square(\delta\boldsymbol{u}^{\mathrm{s}}) + \boldsymbol{\lambda}_g \cdot \bar{\boldsymbol{g}}_\square(\delta\boldsymbol{u}^{\mathrm{s}}), \\
= \frac{1}{A_\square}\int_{\gamma_\square} \boldsymbol{t}_{\mathrm{p}} \cdot \delta\boldsymbol{u}^{\mathrm{s}}\mathrm{d}\Gamma \quad \forall \delta\boldsymbol{u}^{\mathrm{s}} \in \mathbb{U}_\square^{\mathrm{NBC}}, \\
\delta\boldsymbol{\lambda}_\theta \cdot \bar{\boldsymbol{\theta}}_\square(\boldsymbol{u}^{\mathrm{s}}) = 0 \quad \forall \delta\boldsymbol{\lambda}_\theta \in \mathbb{R}^2, \\
\delta\boldsymbol{\lambda}_h : \bar{\boldsymbol{h}}_\square(\boldsymbol{u}^{\mathrm{s}}) = 0 \quad \forall \delta\boldsymbol{\lambda}_h \in \mathbb{R}^{2\times 2}, \\
\delta\boldsymbol{\lambda}_\kappa : \bar{\boldsymbol{\kappa}}_\square(\boldsymbol{u}^{\mathrm{s}}) = 0 \quad \forall \delta\boldsymbol{\lambda}_\kappa \in \mathbb{R}^{2\times 2}, \\
\delta\boldsymbol{\lambda}_g \cdot \bar{\boldsymbol{g}}_\square(\boldsymbol{u}^{\mathrm{s}}) = 0 \quad \forall \delta\boldsymbol{\lambda}_g \in \mathbb{R}^2,
\end{aligned}
\tag{63}
$$

where

$$
\mathbb{U}_\square^{\mathrm{NBC}} = \{\boldsymbol{v} \in [\mathbb{H}^1(\Omega_\square)]^2 : \int_{\Omega_\square} \boldsymbol{v}\mathrm{d}\Omega = 0\}. \tag{64}
$$

5. Numerical examples

In this section, four numerical examples will be presented to demonstrate the effectiveness of the proposed multi-scale framework. The first numerical example aims to verify the framework by comparing predicted plate stiffnesses with analytical results from standard plate theory. The second example investigates the stresses predicted on the SVE-level in an multi-layered composite structure. The third example considers statistical sampling of heterogeneous SVEs with hard spherical inclusions, with the purpose to assess the convergence of the effective plate properties for increasing SVE size in the case of in-plane subscale heterogeneity. The final example considers homogenisation of a unit cell of a 3D woven composite, with the purpose of evaluating the accuracy of the up-scaling plate properties.

In all numerical examples, the homogenised plate stiffness properties will be computed and analysed. In the case of linear elasticity, these can be obtained via the relationship (assuming $\boldsymbol{t}^p = \boldsymbol{0}$):

$$
\begin{aligned}
\bar{\boldsymbol{N}} &= \bar{\boldsymbol{D}}^{\varepsilon,\varepsilon} : \bar{\boldsymbol{\varepsilon}} + \bar{\boldsymbol{D}}^{\varepsilon,\gamma} \cdot \bar{\boldsymbol{\gamma}} + \bar{\boldsymbol{D}}^{\varepsilon,\kappa} : \bar{\boldsymbol{\kappa}}, \\
\bar{\boldsymbol{V}} &= \bar{\boldsymbol{D}}^{\gamma,\varepsilon} : \bar{\boldsymbol{\varepsilon}} + \bar{\boldsymbol{D}}^{\gamma,\gamma} \cdot \bar{\boldsymbol{\gamma}} + \bar{\boldsymbol{D}}^{\gamma,\kappa} : \bar{\boldsymbol{\kappa}}, \\
-\bar{\boldsymbol{M}} &= \bar{\boldsymbol{D}}^{\kappa,\varepsilon} : \bar{\boldsymbol{\varepsilon}} + \bar{\boldsymbol{D}}^{\kappa,\gamma} \cdot \bar{\boldsymbol{\gamma}} + \bar{\boldsymbol{D}}^{\kappa,\kappa} : \bar{\boldsymbol{\kappa}},
\end{aligned}
\tag{65}
$$

where $\bar{\boldsymbol{D}}^{\bullet,\bullet}$ are the plate stiffness properties. As an example, by running a linear SVE-problem with the macro-scale input $\bar{\varepsilon}_{11} = 1$ (and $\bar{\varepsilon}_{12} = \bar{\varepsilon}_{21} = \bar{\varepsilon}_{22} = 0$, $\bar{\boldsymbol{\kappa}} = \boldsymbol{0}$, $\bar{\boldsymbol{\gamma}} = \boldsymbol{0}$), we obtain the plate stiffness components as $\bar{D}^{\varepsilon,\varepsilon}_{\alpha\beta 11} = \bar{N}_{\alpha\beta}$, $\bar{D}^{\gamma,\varepsilon}_{\alpha 11} = \bar{V}_\alpha$ and $\bar{D}^{\kappa,\varepsilon}_{\alpha\beta 11} = -\bar{M}_{\alpha\beta}$ (with $\alpha = \beta = 1, 2$). A similar procedure can be performed to obtain the remaining plate stiffnesses. For more information about the relation in Eq. (65), see Appendix C.

5.1. Verification using homogeneous and isotropic material

In this numerical example, we consider homogenisation of a 3D SVE with homogeneous and linear elastic material. The aim of the study is to verify the proposed computational framework against results from standard plate theory. Specifically, the membrane stiffness $\bar{D}^{\varepsilon,\varepsilon}_{1111}$, bending stiffness $\bar{D}^{\kappa,\kappa}_{1111}$, transverse shear stiffness $\bar{D}^{\gamma\gamma}_{11}$ and symmetrical part of the torsional stiffness $\bar{D}^{\kappa,\kappa}_{1212}$ have been selected to be compared with analytical results.

In this example, the Young's modulus and Poisson's of the material of the sub-structure are set to 210 GPa and 0.3, respectively. The height of the SVE is set to 1 mm, while the equidistant in-plane length and width will vary in order to demonstrate that the proposed framework does not show a pathological dependence on the SVE-size. Finally, periodic boundary conditions (Section 4.1) and enriched periodic boundary conditions (Section 4.2) will be used and compared.

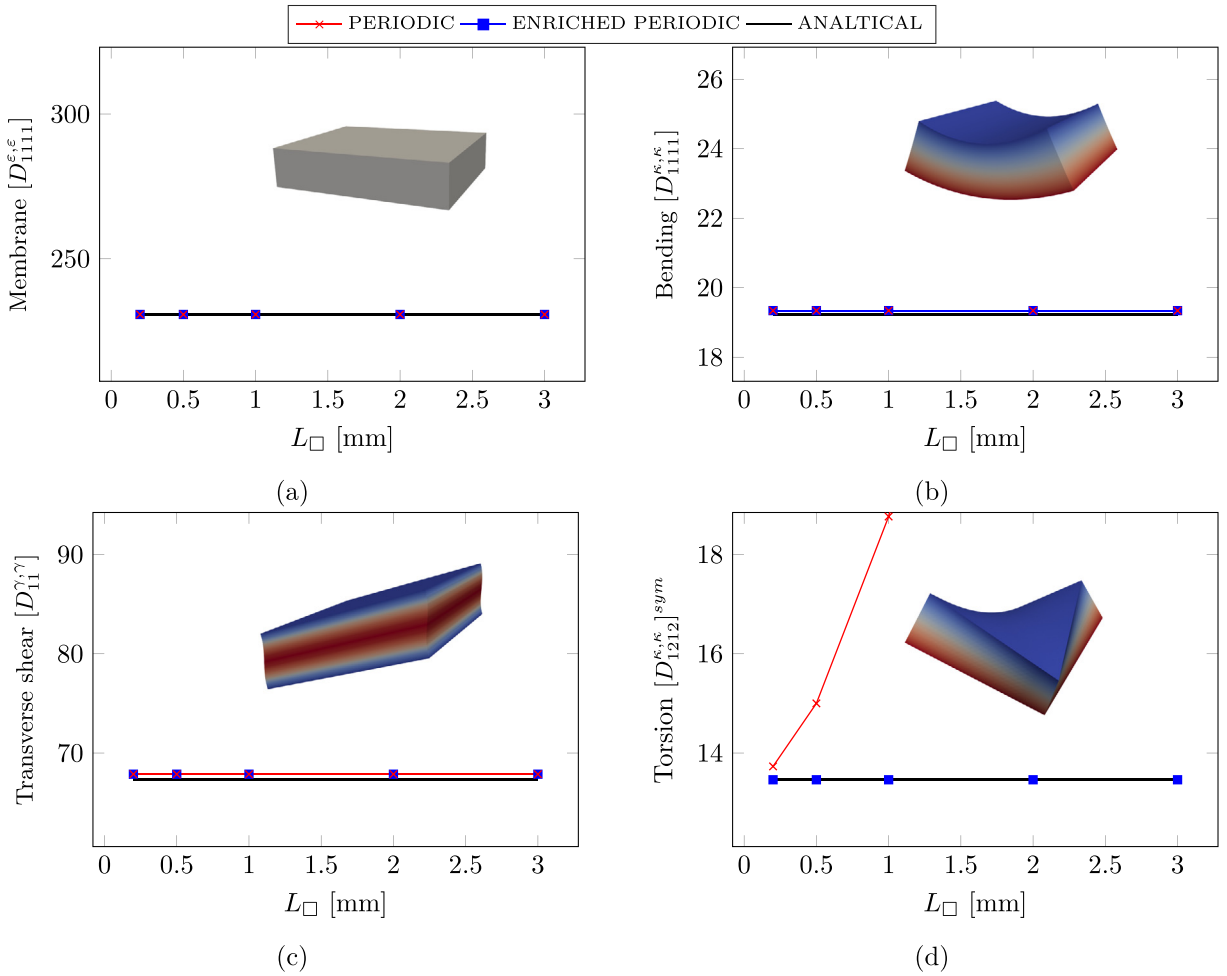

Fig. 5. Resulting sectional forces for a homogeneous SVE, for varying in-plane dimensions of the SVE. The visualised deformation are obtained with the enriched periodic boundary conditions.

The resulting sectional stiffnesses, for varying in-plane dimensions of the SVE, are shown in Fig. 5. The resulting membrane, bending and transverse shear stiffnesses predicted with periodic and enriched periodic boundary conditions show good agreement with the analytical counterparts (here, the analytical shear stiffness includes a correction with the standard shear correction factor 5/6). However, from Fig. 5(d) it is evident that the periodic boundary conditions are unable to accurately predict the torsional stiffness (see Section 4.2 for a discussion). Note, however, that the torsional stiffness matches the analytical solution as the in-plane SVE-size tends towards 0, i.e. when framework coincides with Reissner-Mindlin theory. In contrast, the results with enriched periodic boundary conditions show an accurate prediction of the torsional stiffness also for finite SVE sizes.

In summary, while the (standard) periodic boundary conditions yield good results in most cases, the SVE-problem should in general be modelled with the enriched periodic boundary conditions in order to ensure that all major deformation modes are accurately captured.

5.2. Stress analysis of layered structure

In this numerical example, we will study a multi-layered cantilever beam (narrow plate) with non-symmetric cross-ply layup. The aim of the investigation is to analyse the stresses predicted by the proposed homogenisation framework on the sub-scale level. To do so, a two-scale modelling approach is adopted. The macro-scale is

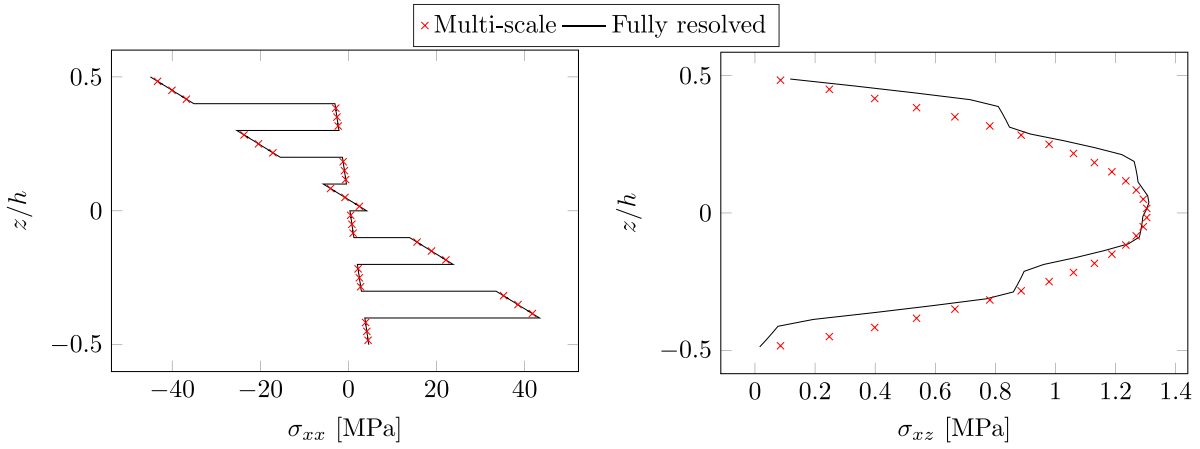

(a) Normal stress (b) Transverse shear stress

Fig. 6. Resulting through-thickness normal and transverse shear stresses at the centre of a multi-layered cantilever beam.

modelled using plate elements, whereas the sub-scale SVE is discretised by standard continuum elements to properly resolve each individual layer in the cross-ply material. The plate elements are formulated using the macro-scale problem derived in Section 3, while the SVE-problem is driven by the micro-periodic boundary conditions (defined in Section 4.1). The resulting stresses from the two-scale formulation are compared to that of a fully resolved simulation modelled with standard continuum elements.

The cantilever beam problem to be analysed consists of a cross-ply laminate with 10 layers: $[90°/0°]_5$ (where $0°$ is aligned with length direction of the beam). The dimensions of the beam are $100 \times 20 \times 10$ mm in the length, width and height direction, respectively. Moreover, the individual plies are assumed to be transversely isotropic, with the following values: $E_L = 120 \times 10^3$ MPa, $E_T = 10.5 \times 10^3$ MPa, $G_{LT} = 5.25 \times 10^3$ MPa, $\nu_{LT} = 0.3$ and $\nu_{TT'} = 0.51$. Finally, the beam is subjected to an edge-load of 175 N.

The fully resolved simulation consists of $50 \times 5 \times 40$ standard continuum elements in the length, width and height directions, respectively (four elements per layer). The two-scale simulation on the other hand, consists of 50×5 plate elements in the length and width directions, while the fine-scale SVE model consists of 30 elements in out-of-plane direction (note that the solution is independent of the in-plane discretisation due the periodic boundary conditions and homogeneity in the in-plane direction).

In Fig. 6, the normal stress (along the beam), denoted σ_{xx}, and the transverse shear stress, denoted σ_{xz}, have been plotted through the thickness at the centre of the beam. The results indicate good agreement between the two-scale approach and the fully resolved model in predicting the normal stress distribution. However, the two-scale approach predicts a purely parabolic distribution of the transverse shear stress through the thickness. Thereby, it does not fully capture the finer variations seen at the interfaces in the fully resolved simulation. Notwithstanding, an analysis of the average shear force obtained from both models indicates that they both predict a similar value of 8.7 N/mm, suggesting that the overall shear-stiffness of the structure is accurately captured by the two-scale approach.

To conclude this example, it is found that the proposed homogenisation framework can capture the average transverse shear response of a layered structure well, however, does not fully capture the fine-scale variations of the transverse shear stresses through the thickness of the SVE. This shortcoming is attributed to the volumetric constraint emanating from $\bar{\boldsymbol{\theta}}_\square$ in Eq. (45), which results in a distributed body load that impacts the equilibrium state of the SVE (in terms of $\boldsymbol{\lambda}_\theta$).

5.3. Statistical sampling of 3D SVEs with spherical inclusions

In this numerical example, we will consider computational homogenisation of a heterogeneous sub-scale structure with hard spherical inclusions embedded in a soft matrix material. The aim of the numerical study is to demonstrate

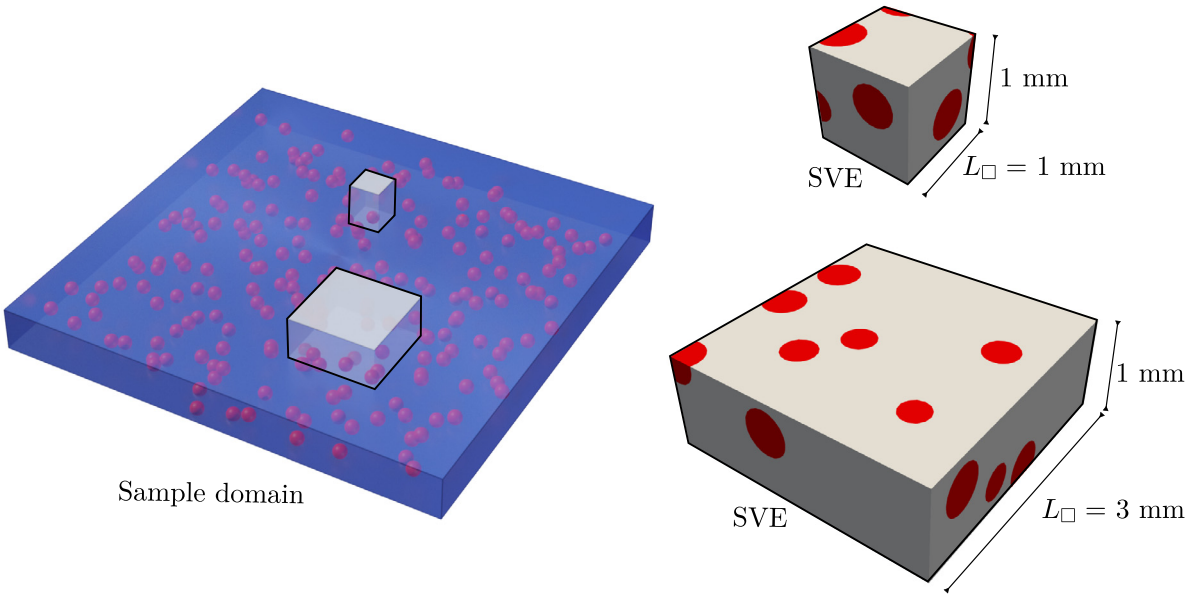

Fig. 7. A heterogeneous domain with spherical inclusions embedded within a soft matrix. The domain acts a sampling domain from which the SVE are randomly sampled.

the convergence of the homogenised sectional stiffness properties (Eq. (65)) for a heterogeneous material. As such, the components $\bar{D}^{\varepsilon,\varepsilon}_{1111}$, $\bar{D}^{\kappa,\kappa}_{1111}$, $\bar{D}^{\gamma,\gamma}_{11}$ and $\bar{D}^{\kappa,\kappa}_{1212}$ will be computed and evaluated, for varying size of the SVE.

To ensure that a statistical representativeness of the sub-scale is captured, multiple statistical volume elements with identical volume fractions are generated for each SVE-size, by a randomised sampling process from a larger "sampling" domain, shown in Fig. 7. The size of the sampling domain is $50 \times 50 \times 1$ mm ($L \times W \times H$). Moreover, the in-plane length and width of the SVEs, here denoted $L_\square$, will vary between 0.1 mm and 3 mm, while the height will be kept constant at 1 mm (i.e. the full height of the sample domain).

The spherical inclusions of the sub-structure are assumed to be linearly elastic with Young's modulus $E = 100$ GPa and Poisson's ratio 0.3, and occupy 17 percent of the total volume. Moreover, the radius of the inclusions are set to 0.2 mm. The matrix material is chosen to be linearly elastic, with Young's modulus $E = 10$ GPa and Poisson's ratio 0.3.

The resulting mean and standard deviation of $\bar{D}^{\varepsilon,\varepsilon}_{1111}$, for different SVE sizes, are shown in Figs. 8(a) and 8(b), respectively. Moreover, the deformation is shown in Fig. 9(a). As a first observation, it can be noted that the standard deviation is large for small SVE sizes, since a small SVE do not include the relevant statistical representation of the sub-structure (in the in-plane directions). In contrast, large SVEs are able to capture the in-plane heterogeneity statistics and the standard deviation is therefore smaller (tends towards zero). It can also be noted that the mean of $\bar{D}^{\varepsilon,\varepsilon}_{1111}$ converges to the same value for all boundary conditions. This is to be expected, since the boundary has a decreasing influence on the results for increasing domain sizes.

The homogenised value of the bending stiffness $\bar{D}^{\kappa,\kappa}_{1111}$, when the SVE is subjected to pure bending, is shown in Fig. 8(c) and 8(d), while the deformation is shown in Fig. 9(b). A similar observation as for the homogenisation of $\bar{D}^{\varepsilon,\varepsilon}_{1111}$ can be made here; a sufficiently large SVE is required to capture the heterogeneities in the in-plane dimension. Moreover, a shortcoming for the results obtained with Dirichlet boundary conditions can be seen in Fig. 8(c). This is caused by an over-constraining from the Dirichlet boundary condition on the lateral faces of the SVE, as previously discussed in Section 4.4. A detailed discussion and proposed remedy to this issue can be found in Appendix B.

With regard to the symmetrical part of the torsional stiffness $\bar{D}^{\kappa,\kappa}_{1212}$ presented in Fig. 8(e), similar conclusions can be drawn as for the case with homogeneous SVE; the periodic and Dirichlet boundary conditions prohibit the SVE to deform anti-periodically, thereby causing an overestimation of the torsional stiffness for increasing size of the SVE. The enriched periodic, Neumann and Dirichlet boundary conditions, however, possess the out-of-plane flexibility needed to properly capture the torsional deformation mode, and the predicted torsional stiffness therefore converges for large SVEs.

Finally, in Fig. 8(g) and 8(h), it is shown that also the transverse shear stiffness $\bar{D}^{\gamma,\gamma}_{11}$ converges to a unique value for increasing SVE sizes, and no pathological size dependency can be seen. Thus, it can be concluded that the proposed method can properly account for the statistics of in-plane heterogeneities, and shows no spurious sensitivity to an increasing SVE size, for all three idealised deformation modes.

5.4. Upscaling of beam properties of 3D woven composite

In this numerical example, we aim to verify the up-scaling capabilities of the proposed homogenisation framework by considering the accuracy of the up-scaled plate stiffness properties from a more complex sub-scale meso-structure. To do so, we consider a periodic unit cell that represents the interior sub-structure of a fibre composite reinforced with a 3D-woven yarn architecture, see Fig. 10 . As such, the unit cell consists of yarns in the warp, horizontal weft, and vertical weft directions, embedded in a polymeric matrix material. Furthermore, the unit cell is slender, whereby a consistent a homogenisation framework, such as the one presented herein, is crucial for accurately estimating its transverse shear behaviour.

The geometry and finite element mesh of the unit cell has been developed in Stig et al. [24], with methodology described in [25], and has been further analysed in the works by Oddy et al. [26]. The unit cell contains local and spatially varying information about the fibre orientations and the volume fractions. Moreover, the unit cell has a length of $L_x = 11.74$ mm, and a height and width of $L_y = L_z = 2.18$ mm. For detailed information about the nominal fibre volume fraction in the yarns, the material parameters for the fibres and the matrix, as well as the micromechanical model used to predict spatially varying yarn properties, please see [24].

To assess the accuracy of the up-scaled plate stiffness properties, the case of a cantilever beam is analysed. Here, a Timoshenko beam solution with stiffness properties up-scaled from the unit cell will be compared against the results from a direct numerical simulation (in which the beam heterogeneity is explicitly modelled). The reason for choosing to analyse a beam, as opposed to a plate, is to make a comparison with a direct numerical simulation feasible, without excessive computational cost.

The beam problem to be analysed is a cantilever beam with an edge load set to 10 N. The total length of the beam is two times the length of the unit cell, while the width and height is equal to that of the unit cell. The top and bottom surfaces of the beam are assumed to free.

The effective membrane stiffness $\overline{EA}$, bending stiffness $\overline{EI}$ and shear stiffness $\overline{KGA}$ used in the Timoshenko beam model are evaluated as

$$\overline{EA} = L_y \bar{D}^{\varepsilon,\varepsilon}_{1111} = 315959 \text{ N}, \tag{66}$$

$$\overline{EI} = L_y \bar{D}^{\kappa,\kappa}_{1111} = 105442 \text{ Nmm}^2, \tag{67}$$

$$\overline{KGA} = L_y \bar{D}^{\gamma,\gamma}_{111} = 16047 \text{ N}, \tag{68}$$

where $\bar{D}^{\varepsilon,\varepsilon}_{1111}$, $\bar{D}^{\kappa,\kappa}_{1111}$ and $\bar{D}^{\gamma,\gamma}_{111}$ are obtained as homogenised quantities resulting from the SVE boundary value problem with periodic boundary conditions. Note that, since the current homogenisation framework is developed for plates, the homogenised beam quantities are obtained under the assumption that the homogenised in-plane transverse strain is constrained ($\bar{\varepsilon}_{22} = 0$). This is a stiffer assumption then what is typically used for beams where the lateral surfaces are free ($\bar{\sigma}_{22} = 0$), however, this does not create a noticeable effect the current results.

In Fig. 11, the vertical displacement along the centre line of the beam is presented for both the fully resolved and the Timoshenko beam simulations. Both solutions show excellent agreement with each other, indicating that the homogenisation framework accurately predicts the stiffness properties of the unit cell, thereby verifying the accuracy of the two-scale method.

6. Conclusions

In this work, we have proposed a consistent homogenisation framework for plate elements, and demonstrated its particular application to a Reissner–Mindlin kinematic model. The proposed framework, based on the Variationally Consistent Homogenisation method, which guarantees kinematic consistency between the macro- and sub-scale. Furthermore, the proposed homogenisation framework is general, free from any a-priori assumptions on each of the

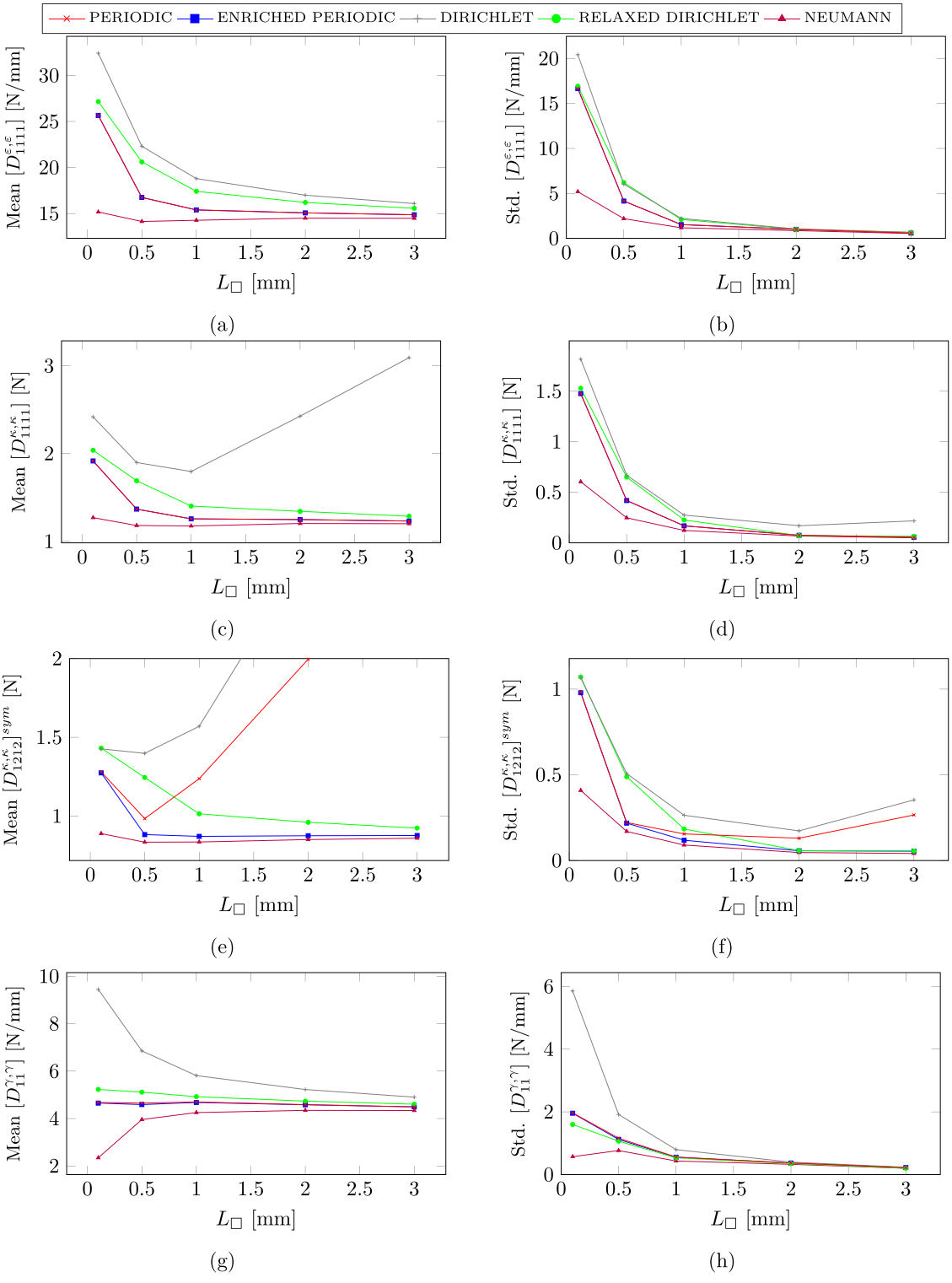

Fig. 8. Resulting homogenised sectional forces as a function of SVE size.

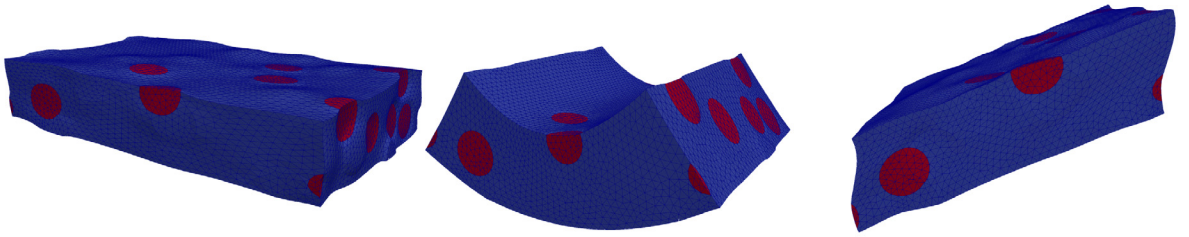

(a) $\bar{\varepsilon}_{11}$ (b) $\bar{\kappa}_{11}$ (c) $\bar{g}_{11}$

Fig. 9. Resulting deformations for a SVE (with periodic boundary conditions).

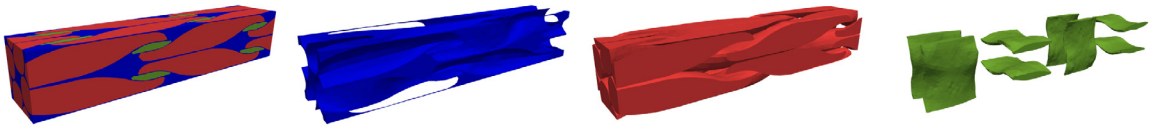

(a) The full Unit cell. (b) Matrix. (c) Warp yarns. (d) Weft yarns.

Fig. 10. A unit cell of an 3D woven composite.

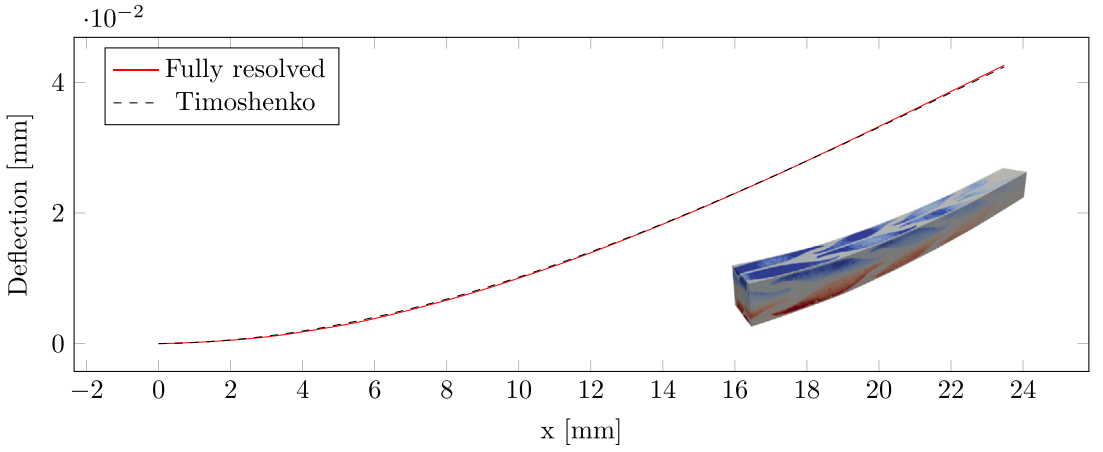

Fig. 11. The resulting displacement field along the centre line of the cantilever beam.

considered scales, and can be efficiently applied to any sub-scale structure and material behaviour, prior to macroscopic localisation, to establish constitutive relations for membrane, bending, and transverse shear deformation modes.

Following the method of VCH, the macro-scale and sub-scale problems are both derived from a single, fully resolved problem. As a direct consequence, the macro-scale problem can be identified as the classical weak form of the classical Reissner-Mindlin plate theory, although with the constitutive relations for the membrane, bending and transverse shear behaviour being determined from the sub-scale (SVE) problem. Moreover, the SVE problem constitutes a standard continuum formulation, with a set of constraints enforcing the kinematical equivalence to the macro-scale. Most notably, it has been demonstrated that, an internal volume constraint appears from the derivations. This constraint is necessary to enforce an effective (volume-averaged) shear angle throughout the SVE volume. This constraint counteract the spurious transverse shear modes that otherwise would appear in plate-based computational homogenisation.

In the section that presents the numerical examples, we validate and demonstrate the accuracy of the framework. First, we investigate the accuracy of the proposed method for a homogeneous and linear elastic SVE, where the results can be compared with classical Reissner-Mindlin plate theory. Here, it can be concluded that SVE-problem modelled with periodic boundary conditions accurately predicts membrane, bending and transverse shear stiffnesses, however, shows erroneous predictions for the torsional stiffness. This issue is overcome with the enriched periodic boundary conditions, which are proposed in Section 4.2. It can be concluded the standard periodic boundary conditions yield good results in the majority of deformation modes, however enriched periodic boundary conditions should in general be favoured.

In the second numerical example, a multi-scale simulation of a layered cantilever beam (modelled as a narrow plate) is performed, and compared with a reference solution obtained from a fully resolved simulation. By studying the predicted transverse shear stresses through the thickness of the beam, it is demonstrated that the sub-scale SVE solution captures the general parabolic shape of the transverse shear stress, but lacks some capability to fully resolve the finer details seen in the reference simulation.

In the third numerical example, we show that the method can properly account for the statistics of in-plane heterogeneities, and shows no spurious sensitivity to an increasing SVE size. We also analyse the performance of different types of sub-scale boundary conditions, and show that results from both Neumann and relaxed Dirichlet conditions converge to the same values as results obtained with periodic boundary conditions as the SVE size increase. In the last example, we demonstrate the up-scaling capabilities of the method in the practical case of a polymer reinforced with a 3D-woven yarn architecture. In particular, we show that the results obtained from a simple Timoshenko beam model, with beam properties up-scaled from SVE computations, is practically identical to the results obtained through a direct numerical simulation of a model where the meso-structure is fully resolved.

In summary, the numerical results show how the proposed two-scale modelling approach can be used to enhance the predictive capabilities of plate models when sub-structural features have a significant influence on the macro-scale behaviour. An important feature is that the proposed approach consistently handles SVEs of increasing in-plane size, which stems from the enforcement of constraints on the volume averaged transverse shear angles of the SVE to be equal to the macro-scopic counter-parts. Although, the enforcement of these volume constraints introduces an additional distributed body load that impacts the equilibrium state of the SVE, and thereby possibly also the detailed distribution of sub-scale stresses (see example 2), the benefit of allowing a consistent treatment of larger in-plane sizes of SVEs is considered to be of superior importance. Thereby, we believe that, combined with the incorporation of proper nonlinear material behaviour on the sub-scale, the proposed framework can be used to explain the sequence of inelastic and damage modes leading up to final failure of complex, thin walled components with intricate material sub-structures.

Declaration of competing interest

The authors declare that they have no known competing financial interests or personal relationships that could have appeared to influence the work reported in this paper.

Data availability

Data will be made available on request

Acknowledgements

The work in this paper has been funded by the Swedish Research Council through grant no. 2018-05345. Financial support has in part also been provided by Vinnova's strategic innovation programme LIGHTer, Sweden (LIGHTer Academy grant no. 2020-04526).

Appendix A. Derivations of gradients of homogenisation operators

In order to ensure that the homogenisation operator $\bar{\boldsymbol{h}}_{\square}(\boldsymbol{u})$ is kinematically coupled to $\bar{\boldsymbol{u}}_{\square}(\boldsymbol{u})$ (i.e $\bar{\boldsymbol{h}} = \bar{\boldsymbol{h}}_{\square}$ should represent the gradient of $\bar{\boldsymbol{u}} = \bar{\boldsymbol{u}}_{\square}$ for a given field $\boldsymbol{u}(\boldsymbol{x})$), it is possible to choose $\bar{\boldsymbol{h}}_{\square}$ as the sensitivity of $\bar{\boldsymbol{u}}_{\square}$ with respect to the placement of the SVE-window, as illustrated in Fig. A.1.

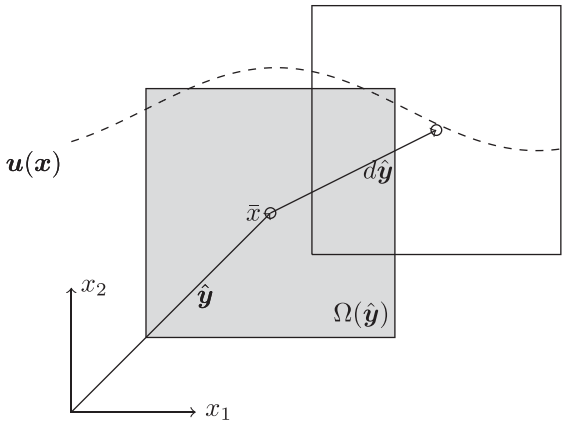

Fig. A.1. Illustration of the operation performed in Eq. (22). The sensitivity is taken w.r.t the position of the SVE-window $\Omega_\square(\hat{\boldsymbol{y}})$.

Let $\hat{\boldsymbol{y}}$ denote the placement of the SVE-volume, $\Omega_\square(\hat{\boldsymbol{y}})$. The sensitivity of $\bar{\boldsymbol{u}}_\square(\hat{\boldsymbol{y}};\boldsymbol{u}) = \frac{1}{\Omega_\square}\int_{\Omega_\square(\hat{\boldsymbol{y}})}(\hat{\boldsymbol{I}}\cdot\boldsymbol{u}(\boldsymbol{x}))\mathrm{d}\Omega$ w.r.t. to $\hat{\boldsymbol{y}}$ is then evaluated as follows:

$$\bar{\boldsymbol{h}}_\square(\bar{\boldsymbol{x}};\boldsymbol{u}) = \bar{\boldsymbol{u}}_\square(\hat{\boldsymbol{y}};\boldsymbol{u})\otimes\hat{\boldsymbol{\nabla}}_{\hat{y}}\big|_{\hat{\boldsymbol{y}}=\bar{\boldsymbol{x}}} = \frac{1}{\Omega_\square}\int_{\Omega_\square(\hat{\boldsymbol{y}})}(\hat{\boldsymbol{I}}\cdot\boldsymbol{u}(\boldsymbol{x}))\mathrm{d}\Omega\otimes\hat{\boldsymbol{\nabla}}_{\hat{y}} \quad \text{evaluated at } \hat{\boldsymbol{y}}=\bar{\boldsymbol{x}}. \tag{A.1}$$

Using Reynolds transport theorem on the last expression in the equation above, and evaluating $\hat{\boldsymbol{y}}=\bar{\boldsymbol{x}}$, we get

$$\begin{aligned}\bar{\boldsymbol{h}}_\square(\bar{\boldsymbol{x}};\boldsymbol{u}) &= \frac{1}{\Omega_\square}\int_{\partial\Omega(\bar{\boldsymbol{x}})}(\hat{\boldsymbol{I}}\cdot\boldsymbol{u})\otimes(\hat{\boldsymbol{I}}\cdot\boldsymbol{n})\mathrm{d}\Gamma\\ &= \frac{1}{\Omega_\square}\int_{\Gamma_\square(\bar{\boldsymbol{x}})}\hat{\boldsymbol{I}}\cdot\boldsymbol{u}\otimes\boldsymbol{n}\mathrm{d}\Gamma\end{aligned} \tag{A.2}$$

where we used the fact that $\hat{\boldsymbol{I}}\cdot\boldsymbol{n}=\boldsymbol{0}$ on $\gamma_\square$ and $\hat{\boldsymbol{I}}\cdot\boldsymbol{n}=\boldsymbol{n}$ on $\Gamma_\square$. Furthermore, by making use of the periodic mapping $\boldsymbol{\varphi}^{\mathrm{PER}}:\Gamma_\square^+\to\Gamma_\square^-$ and jump-operator $[\![\bullet]\!]$, and the fact that the $\boldsymbol{n}$ on $\Gamma_\square^+$ and $\Gamma_\square^-$ are opposite, we obtain the final expression presented in Eq. (22):

$$\bar{\boldsymbol{h}}_\square(\bar{\boldsymbol{x}};\boldsymbol{u}) = \frac{1}{\Omega_\square}\int_{\Gamma_\square(\bar{\boldsymbol{x}})}\hat{\boldsymbol{I}}\cdot\boldsymbol{u}\otimes\boldsymbol{n}\mathrm{d}\Gamma = \frac{1}{\Omega_\square}\int_{\Gamma_\square^+(\bar{\boldsymbol{x}})}\hat{\boldsymbol{I}}\cdot[\![\boldsymbol{u}]\!]\otimes\boldsymbol{n}\mathrm{d}\Gamma \tag{A.3}$$

A similar procedure can be performed for $\bar{\boldsymbol{\kappa}}_\square(\boldsymbol{u})$ and $\bar{\boldsymbol{g}}_\square(\boldsymbol{u})$.

Appendix B. Extended prolongation

In the section with numerical examples we highlight two issues; *(i)* the inability to capture the torsional stiffness of the SVE when modelled with periodic boundary conditions, and *(iii)* the overestimation of the SVE bending stiffness when modelled with Dirichlet boundary conditions. Both these shortcomings can be attributed to the lack of higher order deformation terms in the prolongation $\boldsymbol{u}^{\mathrm{M}}$. As such, we here propose a remedy by extending the prolongation $\boldsymbol{u}^{\mathrm{M}}$ in Eq. (14), by adding higher order terms that include bending and torsional modes. In particular, the proposed extended prolongation is:

$$\begin{aligned}\boldsymbol{u}^{\mathrm{M}}(\hat{\boldsymbol{x}},z) = {}& \bar{\boldsymbol{u}}(\bar{\boldsymbol{x}}) + \bar{\boldsymbol{h}}(\bar{\boldsymbol{x}})\cdot[\hat{\boldsymbol{x}}-\bar{\boldsymbol{x}}] - z\bar{\boldsymbol{\theta}}(\bar{\boldsymbol{x}}) - z\bar{\boldsymbol{\kappa}}(\bar{\boldsymbol{x}})\cdot[\hat{\boldsymbol{x}}-\bar{\boldsymbol{x}}] + \bar{w}(\bar{\boldsymbol{x}})\boldsymbol{e}_3 + \bar{\boldsymbol{g}}(\bar{\boldsymbol{x}})\cdot[\hat{\boldsymbol{x}}-\bar{\boldsymbol{x}}]\boldsymbol{e}_3\\ &+ \frac{1}{2}\left([\hat{\boldsymbol{x}}-\bar{\boldsymbol{x}}]\cdot\bar{\boldsymbol{\kappa}}\cdot[\hat{\boldsymbol{x}}-\bar{\boldsymbol{x}}]\right)\boldsymbol{e}_3 - \frac{1}{2}\langle[\hat{\boldsymbol{x}}+\bar{\boldsymbol{x}}]\cdot\bar{\boldsymbol{\kappa}}\cdot[\hat{\boldsymbol{x}}-\bar{\boldsymbol{x}}]\rangle_\square\boldsymbol{e}_3 \quad \text{in} \quad \Omega_\square,\end{aligned} \tag{B.1}$$

where the first row is identical to the initial prolongation proposed in Section 2.4, and the second row contains extension with the higher order terms. Here, the first term contains a quadratic part of the placement $\hat{\boldsymbol{x}}$, which encodes a bending and torsional deformation mode in the out-of-plane direction. These macro-scopic deformation modes are visualised in Fig. B.1, c.f. Fig. 4. Moreover, the last term is added to remove the translation in z-directions created by the second term. It is important to note that the requirements in Eq. (17) are still satisfied by the new extended prolongation(see Fig. B.2).

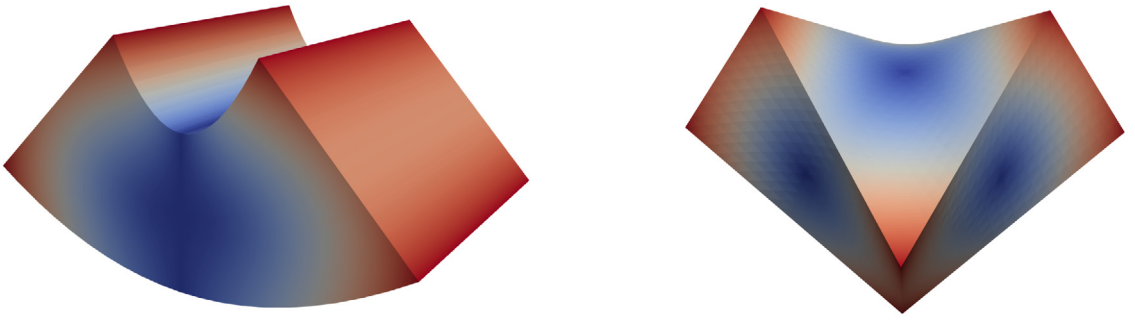

(a) $\kappa_{11} = 1.0$ (b) $\kappa_{12} = \kappa_{21} = 1.0$

Fig. B.1. Visualisation with the prolongation of bending and symmetric twisting modes for the extended $\boldsymbol{u}^{\mathrm{M}}$ in Eq. (B.1) (c.f. Fig. 4).

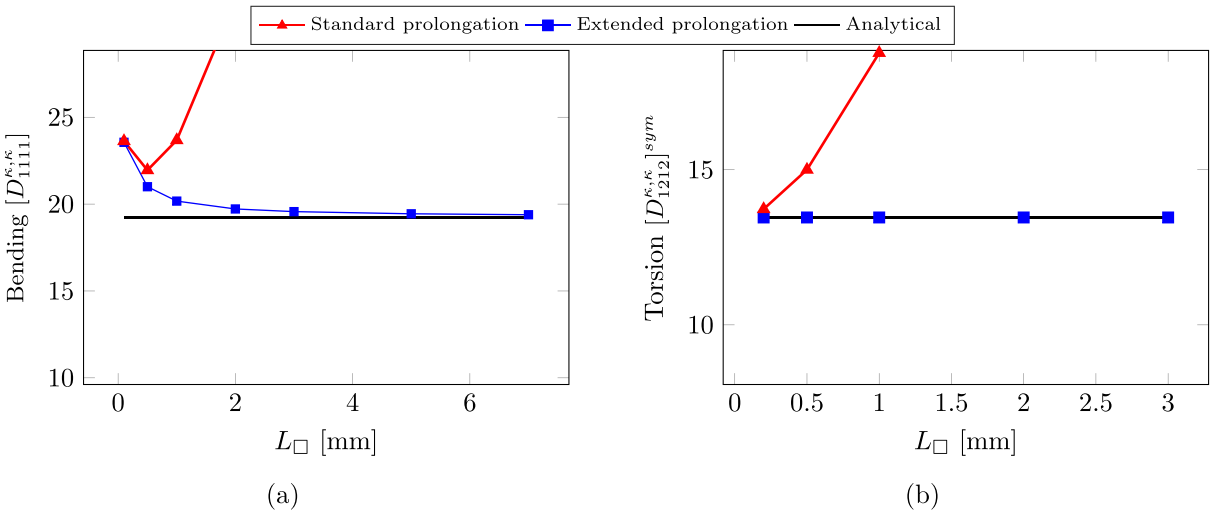

Fig. B.2. Comparison between the standard prolongation (Equation) and extended prolongation (Equation). The left figure shows the bending stiffness when (unmodified) Dirichlet boundary conditions are used, and the right figure shown the torsional stiffness for (unmodified) periodic boundary conditions.

Remark. The addition of the higher order term in Eq. (B.1) creates a slight down-stream effect on the macro-scale boundary value problem. The bending moment $\bar{\boldsymbol{M}}$ is updated as (c.f. Eq. (30)):

$$\bar{\boldsymbol{M}} = \frac{1}{A_\square}\int_{\Omega_\square} z\left(\hat{\boldsymbol{I}}\cdot\boldsymbol{\sigma}\cdot\hat{\boldsymbol{I}}\right) + \left((\hat{\boldsymbol{I}}\cdot\boldsymbol{\sigma}\cdot\boldsymbol{e}_z)\otimes(\hat{\boldsymbol{x}}-\bar{\boldsymbol{x}})\right)^{\mathrm{skw}} \mathrm{d}\Omega. \tag{B.2}$$

Results with the extended prolongation

We revisit the first study in Section 5.1 (homogeneous and linear elastic SVE) to demonstrate the effectiveness with the proposed extended prolongation. The quantities of interest are; the bending stiffness $\bar{D}^{\kappa\kappa}_{1111}$ (when modelled with Dirichlet boundary conditions), and the symmetric part of the torsional stiffness $\bar{D}^{\kappa\kappa}_{1212}$ (when modelled with standard periodic boundary conditions).

The bending stiffness $\bar{D}^{\kappa\kappa}_{1111}$ of the SVE, when modelled with Dirichlet boundary conditions, are shown in Fig. B.2(a). It can be seen that the bending stiffness is captured as the SVE-size increases and the boundary effects of the Dirichlet conditions decreases.

The torsional stiffness $\bar{D}^{\kappa\kappa}_{1212}$ of the SVE, when modelled with periodic boundary conditions, are shown in Fig. B.2(b). It can be concluded that since the twisting mode is included in the extended prolongation $\boldsymbol{u}^{\mathrm{M}}$, the torsional stiffness is captured for all sizes of the SVE.

Appendix C. On the computation of plate stiffnesses in the linear case

In this appendix, we will derive the expression for the homogenised plate stiffness properties presented in Eq. (65), under the assumption of linear elasticity and no external boundary load ($\boldsymbol{t}_p = \boldsymbol{0}$ on $\gamma_\square$). In such a case, the Cauchy stress can be expressed as $\boldsymbol{\sigma} = \boldsymbol{E} : \boldsymbol{\varepsilon}$, with $\boldsymbol{E}$ denoting the fourth order linear elastic stiffness tensor. Upon introducing this linear relation into Eq. (39), the linear SVE-problem can be stated as that of solving for $\boldsymbol{u}^{\mathrm{s}} \in \mathbb{U}^{\mathrm{s}}_\square$ such that:

$$\frac{1}{A_\square}\int_{\Omega_\square} \boldsymbol{\epsilon}[\delta\boldsymbol{u}^{\mathrm{s}}] : \boldsymbol{E} : \boldsymbol{\epsilon}[\boldsymbol{u}^{\mathrm{s}}]\mathrm{d}\Omega = \frac{1}{A_\square}\int_{\gamma_\square} \boldsymbol{t}_{\mathrm{p}} \cdot \delta\boldsymbol{u}^{\mathrm{s}}\mathrm{d}\Gamma - \frac{1}{A_\square}\int_{\Omega_\square} \boldsymbol{\epsilon}[\delta\boldsymbol{u}^{\mathrm{s}}] : \boldsymbol{E} : \boldsymbol{\epsilon}[\boldsymbol{u}^{\mathrm{M}}]\mathrm{d}\Omega \quad \forall \delta\boldsymbol{u}^{\mathrm{s}} \in \mathbb{U}^{\mathrm{s}}_\square. \tag{C.1}$$

after which the section forces can be computed as follows(cf. Eqs. (28)–(30)):

$$\begin{aligned}
\bar{N}_{\alpha\beta} &= \frac{1}{A_\square}\int_{\Omega_\square} \boldsymbol{E}_{\alpha\beta} : \boldsymbol{E} : \boldsymbol{\epsilon}[\boldsymbol{u}^{\mathrm{s}} + \boldsymbol{u}^{\mathrm{M}}]\mathrm{d}\Omega \\
\bar{V}_{\alpha} &= \frac{1}{A_\square}\int_{\Omega_\square} \boldsymbol{E}_{3\alpha} : \boldsymbol{E} : \boldsymbol{\epsilon}[\boldsymbol{u}^{\mathrm{s}} + \boldsymbol{u}^{\mathrm{M}}]\mathrm{d}\Omega \\
\bar{M}_{\alpha\beta} &= \frac{1}{A_\square}\int_{\Omega_\square} (z\boldsymbol{E}_{\alpha\beta} + (\hat{x}_\beta - \bar{x}_\beta)\boldsymbol{E}_{3\alpha}) : \boldsymbol{E} : \boldsymbol{\epsilon}[\boldsymbol{u}^{\mathrm{s}} + \boldsymbol{u}^{\mathrm{M}}]\mathrm{d}\Omega
\end{aligned} \tag{C.2}$$

where

$$\boldsymbol{E}_{\alpha\beta} = [\boldsymbol{e}_\alpha \otimes \boldsymbol{e}_\beta]^{\mathrm{sym}}, \qquad \boldsymbol{E}_{3\alpha} = [\boldsymbol{e}_3 \otimes \boldsymbol{e}_\alpha]^{\mathrm{sym}}. \tag{C.3}$$

Due to the assumption of linear elasticity, the solution to fluctuation field $\boldsymbol{u}^{\mathrm{s}}$ in Eq. (C.1) can be expressed as a superposition of different deformation modes:

$$\boldsymbol{u}^{\mathrm{s}} = \sum_{\alpha,\beta=0}^{2} \boldsymbol{u}^{s,\varepsilon}_{\alpha\beta}\bar{\epsilon}_{\alpha\beta} + \sum_{\alpha,\beta=0}^{2} \boldsymbol{u}^{s,\gamma}_{\alpha}\bar{\gamma}_{\alpha} + \sum_{\alpha=0}^{2} \boldsymbol{u}^{s,\kappa}_{\alpha\beta}\bar{\kappa}_{\alpha\beta} \tag{C.4}$$

where we formulate for sensitivity problems as

(i) Find $\boldsymbol{u}^{\mathrm{s},\varepsilon}_{\alpha\beta} \in \mathbb{U}^{\mathrm{s}}_\square$ such that for $\alpha, \beta = 1, 2$

$$\frac{1}{A_\square}\int_{\Omega_\square} \boldsymbol{\epsilon}[\delta\boldsymbol{u}^{\mathrm{s}}] : \boldsymbol{E} : \boldsymbol{\epsilon}[\boldsymbol{u}^{\mathrm{s},\varepsilon}_{\alpha\beta}]\mathrm{d}\Omega = -\frac{1}{A_\square}\int_{\Omega_\square} \boldsymbol{\epsilon}[\delta\boldsymbol{u}^{\mathrm{s}}] : \boldsymbol{E} : \boldsymbol{E}_{\alpha\beta}\mathrm{d}\Omega \quad \forall \delta\boldsymbol{u}^{\mathrm{s}} \in \mathbb{U}^{\mathrm{s}}_\square \tag{C.5}$$

(ii) Find $\boldsymbol{u}^{\mathrm{s},\gamma}_{\alpha} \in \mathbb{U}^{\mathrm{s}}_\square$ such that for $\alpha = 1$

$$\frac{1}{A_\square}\int_{\Omega_\square} \boldsymbol{\epsilon}[\delta\boldsymbol{u}^{\mathrm{s}}] : \boldsymbol{E} : \boldsymbol{\epsilon}[\boldsymbol{u}^{\mathrm{s},\gamma}_{\alpha}]\mathrm{d}\Omega = -\frac{1}{A_\square}\int_{\Omega_\square} \boldsymbol{\epsilon}[\delta\boldsymbol{u}^{\mathrm{s}}] : \boldsymbol{E} : \boldsymbol{E}_{3\alpha}\mathrm{d}\Omega \quad \forall \delta\boldsymbol{u}^{\mathrm{s}} \in \mathbb{U}^{\mathrm{s}}_\square \tag{C.6}$$

(iii) Find $\boldsymbol{u}^{\mathrm{s},\kappa}_{\alpha\beta} \in \mathbb{U}^{\mathrm{s}}_\square$ such that for $\alpha, \beta = 1, 2$

$$\frac{1}{A_\square}\int_{\Omega_\square} \boldsymbol{\epsilon}[\delta\boldsymbol{u}^{\mathrm{s}}] : \boldsymbol{E} : \boldsymbol{\epsilon}[\boldsymbol{u}^{\mathrm{s},\kappa}_{\alpha\beta}]\mathrm{d}\Omega = -\frac{1}{A_\square}\int_{\Omega_\square} \boldsymbol{\epsilon}[\delta\boldsymbol{u}^{\mathrm{s}}] : \boldsymbol{E} : \left(-z\boldsymbol{E}_{\alpha\beta} - (\hat{x}_\beta - \bar{x}_\beta)\boldsymbol{E}_{3\alpha}\right)\mathrm{d}\Omega \quad \forall \delta\boldsymbol{u}^{\mathrm{s}} \in \mathbb{U}^{\mathrm{s}}_\square. \tag{C.7}$$

It can be verified that Eqs. (C.4) together with Eqs. (C.5)–(C.7) solves the SVE-problem in Eqs. (C.1). Moreover, in the Eqs. (C.5)–(C.7), we have used that $\boldsymbol{\epsilon}[\boldsymbol{u}^{\mathrm{M}}]$ can be expressed as:

$$\boldsymbol{\epsilon}[\boldsymbol{u}^{\mathrm{M}}] = \sum_{\alpha,\beta=1}^{2} \boldsymbol{E}_{\alpha\beta}\bar{\epsilon}_{\alpha\beta} + \sum_{\alpha=1} E^2_{3\alpha}\bar{\gamma}_{\alpha} + \sum_{\alpha,\beta=1}^{2} \left(-z\boldsymbol{E}_{\alpha\beta} - (\hat{x}_\beta - \bar{x}_\beta)\boldsymbol{E}_{3\alpha}\right)\bar{\kappa}_{\alpha\beta}. \tag{C.8}$$

By inserting the superposition of $\boldsymbol{u}^{\mathrm{s}}$ in Eq. (C.4), into the expressions for the sectional forces in Eq. (C.2), we obtain an expression for the linear plate stiffness properties:

$$\bar{N}_{\alpha\beta} = \sum_{\gamma,\delta=1}^{2} \bar{D}^{\varepsilon,\varepsilon}_{\alpha\beta\gamma\delta}\bar{\epsilon}_{\gamma\delta} + \sum_{\gamma=1}^{2} \bar{D}^{\varepsilon,\gamma}_{\alpha\beta\gamma}\bar{\gamma}_{\gamma} + \sum_{\gamma,\delta=1}^{2} \bar{D}^{\varepsilon,\kappa}_{\alpha\beta\gamma\delta}\bar{\kappa}_{\gamma\delta} \tag{C.9}$$

$$\bar{V}_\alpha = \sum_{\gamma,\delta=1}^{2} \bar{D}^{\gamma,\varepsilon}_{\alpha\beta\gamma}\bar{\epsilon}_{\beta\gamma} + \sum_{\beta=1}^{2} \bar{D}^{\gamma,\gamma}_{\alpha\beta}\bar{\gamma}_\beta + \sum_{\beta,\gamma=1}^{2} \bar{D}^{\gamma,\kappa}_{\alpha\beta\gamma}\bar{\kappa}_{\beta\gamma} \tag{C.10}$$

$$-\bar{M}_{\alpha\beta} = \sum_{\gamma,\delta=1}^{2} \bar{D}^{\kappa,\varepsilon}_{\alpha\beta\gamma\delta}\bar{\epsilon}_{\gamma\delta} + \sum_{\gamma=1}^{2} \bar{D}^{\kappa,\gamma}_{\alpha\beta\gamma}\bar{\gamma}_\gamma + \sum_{\gamma,\delta=1}^{2} \bar{D}^{\kappa,\kappa}_{\alpha\beta\gamma\delta}\bar{\kappa}_{\gamma\delta} \tag{C.11}$$

where the plate stiffness properties $\bar{D}^{\bullet,\bullet}_{\alpha\beta\gamma\delta}$ are computed as:

$$D^{\varepsilon,\varepsilon}_{\alpha\beta\gamma\delta} = \frac{1}{A_\square}\int_{\Omega_\square} \boldsymbol{E}_{\alpha\beta} : \boldsymbol{E} : \left[\boldsymbol{E}_{\gamma\delta} + \boldsymbol{\epsilon}[\boldsymbol{u}^{s,\varepsilon}_{\gamma\delta}]\right] \mathrm{d}\Omega \tag{C.12}$$

$$D^{\varepsilon,\gamma}_{\alpha\beta\gamma} = \frac{1}{A_\square}\int_{\Omega_\square} \boldsymbol{E}_{\alpha\beta} : \boldsymbol{E} : \left[\boldsymbol{E}_{3\gamma} + \boldsymbol{\epsilon}[\boldsymbol{u}^{s,\gamma}_{\gamma}]\right] \mathrm{d}\Omega \tag{C.13}$$

$$D^{\varepsilon,\kappa}_{\alpha\beta\gamma\delta} = \frac{1}{A_\square}\int_{\Omega_\square} \boldsymbol{E}_{\alpha\beta} : \boldsymbol{E} : \left[-z\boldsymbol{E}_{\gamma\delta} - (\hat{x}_\delta - \bar{x}_\delta)\boldsymbol{E}_{3\gamma} + \boldsymbol{\epsilon}[\boldsymbol{u}^{s,\kappa}_{\gamma\delta}]\right] \mathrm{d}\Omega \tag{C.14}$$

$$D^{\gamma,\varepsilon}_{\alpha\beta\gamma} = \frac{1}{A_\square}\int_{\Omega_\square} \boldsymbol{E}_{3\alpha} : \boldsymbol{E} : \left[\boldsymbol{E}_{\beta\gamma} + \boldsymbol{\epsilon}[\boldsymbol{u}^{s,\varepsilon}_{\beta\gamma}]\right] \mathrm{d}\Omega \tag{C.15}$$

$$D^{\gamma,\gamma}_{\alpha\beta} = \frac{1}{A_\square}\int_{\Omega_\square} \boldsymbol{E}_{3\alpha} : \boldsymbol{E} : \left[\boldsymbol{E}_{3\beta} + \boldsymbol{\epsilon}[\boldsymbol{u}^{s,\gamma}_{\beta}]\right] \mathrm{d}\Omega \tag{C.16}$$

$$D^{\gamma,\kappa}_{\alpha\beta\gamma} = \frac{1}{A_\square}\int_{\Omega_\square} \boldsymbol{E}_{3\alpha} : \boldsymbol{E} : \left[-z\boldsymbol{E}_{\beta\gamma} - (\hat{x}_\gamma - \bar{x}_\gamma)\boldsymbol{E}_{3\beta} + \boldsymbol{\epsilon}[\boldsymbol{u}^{s,\kappa}_{\beta\gamma}]\right] \mathrm{d}\Omega \tag{C.17}$$

$$D^{\kappa,\varepsilon}_{\alpha\beta\gamma\delta} = \frac{1}{A_\square}\int_{\Omega_\square} \left[-z\boldsymbol{E}_{\alpha\beta} - (\hat{x}_\beta - \bar{x}_\beta)\boldsymbol{E}_{3\alpha}\right] : \boldsymbol{E} : \left[\boldsymbol{E}_{\gamma\delta} + \boldsymbol{\epsilon}[\boldsymbol{u}^{s,\varepsilon}_{\gamma\delta}]\right] \mathrm{d}\Omega \tag{C.18}$$

$$D^{\kappa,\gamma}_{\alpha\beta\gamma} = \frac{1}{A_\square}\int_{\Omega_\square} \left[-z\boldsymbol{E}_{\alpha\beta} - (\hat{x}_\beta - \bar{x}_\beta)\boldsymbol{E}_{3\alpha}\right] : \boldsymbol{E} : \left[\boldsymbol{E}_{3\gamma} + \boldsymbol{\epsilon}[\boldsymbol{u}^{s,\gamma}_{\gamma}]\right] \mathrm{d}\Omega \tag{C.19}$$

$$D^{\kappa,\kappa}_{\alpha\beta\gamma\delta} = \frac{1}{A_\square}\int_{\Omega_\square} \left[-z\boldsymbol{E}_{\alpha\beta} - (\hat{x}_\beta - \bar{x}_\beta)\boldsymbol{E}_{3\alpha}\right] : \boldsymbol{E} : \left[-z\boldsymbol{E}_{\gamma\delta} - (\hat{x}_\delta - \bar{x}_\delta)\boldsymbol{E}_{3\gamma} + \boldsymbol{\epsilon}[\boldsymbol{u}^{s,\kappa}_{\gamma\delta}]\right] \mathrm{d}\Omega \tag{C.20}$$

In summary, in order to obtain (for example) the membrane stiffness for $\bar{D}^{\varepsilon,\varepsilon}_{\alpha\beta11}$, one should evaluate the expression in Eq. (C.12), with the solution $\boldsymbol{u}^{s,\varepsilon}_{11}$ obtained from Eq. (C.5) (with $\alpha, \beta = 1$). Note, however, that this is equivalent to evaluating the membrane forces $\bar{N}_{\alpha\beta} = \bar{D}^{\varepsilon,\varepsilon}_{\alpha\beta11}$ (cf. Eq. (28)), with a $\boldsymbol{u}^s$ obtained with by solving the (linear) SVE-problem with the macro-scale input $\bar{\varepsilon}_{11} = 1$ (and $\bar{\varepsilon}_{12} = \bar{\varepsilon}_{21} = \bar{\varepsilon}_{22} = 0$, $\bar{\boldsymbol{\kappa}} = \boldsymbol{0}$, $\bar{\boldsymbol{\gamma}} = \boldsymbol{0}$).

References

[1] S. Klarmann, F. Gruttmann, S. Klinkel, Homogenization assumptions for coupled multiscale analysis of structural elements: beam kinematics, Comput. Mech. 65 (2020) 635–661, http://dx.doi.org/10.1007/s00466-019-01787-z.

[2] C. Oddy, R. Bisschop, M. Fagerström, E. Svenning, F. Larsson, J. Främby, On variationally consistent homogenisation for composite structural elements, in: Proc. of the 6th ECCOMAS Thematic Conference on the Mechanical Response of Composites, Eindhoven, The Netherlands, 2017.

[3] J. Hohe, A direct homogenisation approach for determination of the stiffness matrix for microheterogeneous plates with application to sandwich panels, Composites B 34 (7) (2003) 615–626, http://dx.doi.org/10.1016/S1359-8368(03)00063-5.

[4] M.G. Geers, E.W. Coenen, V.G. Kouznetsova, Multi-scale computational homogenization of structured thin sheets, Modelling Simul. Mater. Sci. Eng. 15 (4) (2007) S393, http://dx.doi.org/10.1088/0965-0393/15/4/S06.

[5] E.W.C. Coenen, V.G. Kouznetsova, M.G.D. Geers, Computational homogenization for heterogeneous thin sheets, Internat. J. Numer. Methods Engrg. 83 (8–9) (2010) 1180–1205, http://dx.doi.org/10.1002/nme.2833.

[6] R. Larsson, M. Landervik, A stress-resultant shell theory based on multiscale homogenization, Comput. Methods Appl. Mech. Engrg. 263 (2013) 1–11, http://dx.doi.org/10.1016/J.CMA.2013.04.011.

[7] A.T. Karttunen, J.N. Reddy, J. Romanoff, Two-scale micropolar plate model for web-core sandwich panels, Int. J. Solids Struct. 170 (2019) 82–94, http://dx.doi.org/10.1016/J.IJSOLSTR.2019.04.026.

[8] J. Torabi, J. Niiranen, Microarchitecture-dependent nonlinear bending analysis for cellular plates with prismatic corrugated cores via an anisotropic strain gradient plate theory of first-order shear deformation, Eng. Struct. 236 (2021) 112117, http://dx.doi.org/10.1016/J.ENGSTRUCT.2021.112117.

[9] A.K. Hii, B. El Said, A kinematically consistent second-order computational homogenisation framework for thick shell models, Comput. Methods Appl. Mech. Engrg. 398 (2022) 115136, http://dx.doi.org/10.1016/j.cma.2022.115136.
[10] J. Fish, K. Shek, M. Pandheeradi, M.S. Shephard, Computational plasticity for composite structures based on mathematical homogenization: Theory and practice, Comput. Methods Appl. Mech. Engrg. 148 (1–2) (1997) 53–73, http://dx.doi.org/10.1016/S0045-7825(97)00030-3.
[11] M.G. Geers, V.G. Kouznetsova, W.A. Brekelmans, Multi-scale computational homogenization: Trends and challenges, J. Comput. Appl. Math. 234 (7) (2010) 2175–2182, http://dx.doi.org/10.1016/J.CAM.2009.08.077.
[12] V. Kouznetsova, M.G.D. Geers, W.A.M. Brekelmans, Multi-scale constitutive modelling of heterogeneous materials with a gradient-enhanced computational homogenization scheme, Internat. J. Numer. Methods Engrg. 54 (8) (2002) 1235–1260, http://dx.doi.org/10.1002/nme.541.
[13] D. Heller, F. Gruttmann, Nonlinear two-scale shell modeling of sandwiches with a comb-like core, Compos. Struct. 144 (2016) 147–155, http://dx.doi.org/10.1016/J.COMPSTRUCT.2016.02.042.
[14] J. Främby, J. Brouzoulis, M. Fagerström, Assessment of two methods for the accurate prediction of transverse stress distributions in laminates, Compos. Struct. 140 (2016) 602–611, http://dx.doi.org/10.1016/J.COMPSTRUCT.2015.12.036.
[15] D. Luscher, D. McDowell, C. Bronkhorst, Essential features of fine scale boundary conditions for second gradient multiscale homogenization of statistical volume elements, Int. J. Multiscale Comput. Eng. 10 (5) (2012) 461–486, http://dx.doi.org/10.1615/IntJMultCompEng.2012002929.
[16] M. Müller, K. Simon, G. Friedrich, A new homogenization scheme for beam and plate structures without a priori requirements on boundary conditions, Comput. Mech. 70 (6) (2022) 1167–1187, http://dx.doi.org/10.1007/s00466-022-02219-1.
[17] F. Larsson, K. Runesson, F. Su, Variationally consistent computational homogenization of transient heat flow, Internat. J. Numer. Methods Engrg. 81 (13) (2010) 1659–1686, http://dx.doi.org/10.1002/NME.2747.
[18] R. Bharali, F. Larsson, R. Jänicke, Computational homogenisation of phase-field fracture, Eur. J. Mech. A Solids 88 (2021) 104247, http://dx.doi.org/10.1016/j.euromechsol.2021.104247.
[19] E. Svenning, M. Fagerström, F. Larsson, Computational homogenization of microfractured continua using weakly periodic boundary conditions, Comput. Methods Appl. Mech. Engrg. 299 (2016) 1–21, http://dx.doi.org/10.1016/j.cma.2015.10.014.
[20] V. Tu, F. Larsson, K. Runesson, R. Jänicke, Computational homogenization of the electro-chemically coupled multi-scale transport of Li-ions in structural battery electrolytes, PAMM 20 (1) (2021) e202000138, http://dx.doi.org/10.1002/pamm.202000138.
[21] S. Kaessmair, P. Steinmann, Computational first-order homogenization in chemo-mechanics, Arch. Appl. Mech. 88 (1–2) (2018) 271–286, http://dx.doi.org/10.1007/s00419-017-1287-0.
[22] C. Oddy, R. Bisschop, Multiscale Modelling of Heterogeneous Beams, Chalmers University of Technology, 2017.
[23] T.J. Hughes, G.R. Feijóo, L. Mazzei, J.-B. Quincy, The variational multiscale method—a paradigm for computational mechanics, Comput. Methods Appl. Mech. Engrg. 166 (1) (1998) 3–24, http://dx.doi.org/10.1016/S0045-7825(98)00079-6, URL https://www.sciencedirect.com/science/article/pii/S0045782598000796. Advances in Stabilized Methods in Computational Mechanics.
[24] F. Stig, S. Hallström, A modelling framework for composites containing 3D reinforcement, Compos. Struct. 94 (9) (2012) 2895–2901, http://dx.doi.org/10.1016/j.compstruct.2012.03.009.
[25] F. Stig, S. Hallström, Spatial modelling of 3D-woven textiles, Compos. Struct. 94 (5) (2012) 1495–1502, http://dx.doi.org/10.1016/j.compstruct.2011.12.003.
[26] C. Oddy, T. Ekermann, M. Ekh, M. Fagerström, S. Hallström, F. Stig, Predicting damage initiation in 3D fibre-reinforced composites – The case for strain-based criteria, Compos. Struct. 230 (2019) 111336, http://dx.doi.org/10.1016/j.compstruct.2019.111336.